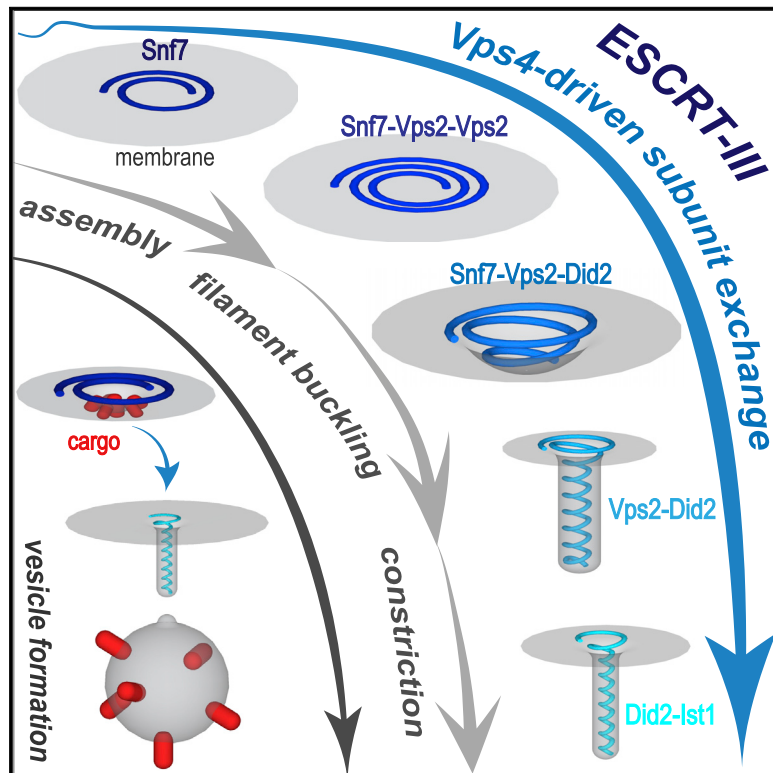**Article**

An ESCRT-III Polymerization Sequence Drives Membrane Deformation and Fission

Graphical Abstract

Authors

Anna-Katharina Pfitzner, Vincent Mercier, Xiuyun Jiang, Joachim Moser von Filseck, Buzz Baum, Anđela Šarić, Aurélien Roux

Correspondence

aurelien.roux@unige.ch

In Brief

The ESCRT-III machinery works by sequential recruitment, polymerization, and replacement of different subunits, resulting in constriction—and, finally, fission—of the membrane.

Highlights

- ESCRT-III subunits polymerize sequentially at the membrane driven by the ATPase Vps4

- The ESCRT-III polymerization sequence ends by Did2/Ist1 to catalyze membrane fission

- Subunit exchange triggers changes in ESCRT-III polymers shape and properties

- Tilt introduction in the polymer-membrane interface mediates filament buckling

CellPress

Article

An ESCRT-III Polymerization Sequence Drives Membrane Deformation and Fission

Anna-Katharina Pfitzner,[1] Vincent Mercier,[1,2] Xiuyun Jiang,[3,4,5] Joachim Moser von Filseck,[1] Buzz Baum,[4,5] Anđela Šarić,[3,4,5] and Aurélien Roux[1,2,6,*]

[1]Department of Biochemistry, University of Geneva, 1211 Geneva, Switzerland
[2]National Center of Competence in Research in Chemical Biology, University of Geneva, 1211 Geneva, Switzerland
[3]Department of Physics and Astronomy, University College London, Gower Street, London WC1E 6BT, UK
[4]Institute for the Physics of Living Systems, University College London, Gower Street, London WC1E 6BT, UK
[5]MRC Laboratory for Molecular Cell Biology, University College London, Gower Street, London WC1E 6BT, UK
[6]Lead Contact
*Correspondence: aurelien.roux@unige.ch
https://doi.org/10.1016/j.cell.2020.07.021

SUMMARY

The endosomal sorting complex required for transport-III (ESCRT-III) catalyzes membrane fission from within membrane necks, a process that is essential for many cellular functions, from cell division to lysosome degradation and autophagy. How it breaks membranes, though, remains unknown. Here, we characterize a sequential polymerization of ESCRT-III subunits that, driven by a recruitment cascade and by continuous subunit-turnover powered by the ATPase Vps4, induces membrane deformation and fission. During this process, the exchange of Vps24 for Did2 induces a tilt in the polymer-membrane interface, which triggers transition from flat spiral polymers to helical filament to drive the formation of membrane protrusions, and ends with the formation of a highly constricted Did2-Ist1 co-polymer that we show is competent to promote fission when bound on the inside of membrane necks. Overall, our results suggest a mechanism of stepwise changes in ESCRT-III filament structure and mechanical properties via exchange of the filament subunits to catalyze ESCRT-III activity.

INTRODUCTION

Eukaryotic cells are characterized by a complex endomembrane system that requires membrane remodeling machineries for its maintenance and dynamics. While it is not known how this endomembrane system evolved, it has been proposed that the endosomal sorting complex required for transport-III (ESCRT-III), which was presumably inherited from archaea during evolution, is essential to the emergence of endomembranes (Baum and Baum, 2014). Uniquely, ESCRT-III has the ability to catalyze membrane fission from within membrane necks and to function on virtually all cellular membranes: it catalyzes formation of intralumenal vesicles (ILVs) from the endosome membrane, cytokinetic abscission of the plasma membrane, reformation of the nuclear envelope, and closure of autophagosomes (Schöneberg et al., 2017). ESCRT-III-mediated membrane fission is also involved in the budding of various virions in eukaryotes and archaea and in repairing the plasma membrane as well as lysosomal and nuclear membranes (Vietri et al., 2020). This repair function was shown to help confine bacterial pathogens to the host vacuole (Vietri et al., 2020). Its ubiquitous role in vital cellular functions defines ESCRT-III as an essential membrane remodeling complex. Understanding how it performs its function is thus critical.

Canonically recruited by ESCRT-II, ESCRT-III assembly starts with Vps20 followed by the core subunits Snf7, Vps2, and Vps24. Vps2 and Vps24 bind Snf7 in tandem and then recruit the AAA-ATPase Vps4 (Babst et al., 2002; Obita et al., 2007; Saksena et al., 2009; Stuchell-Brereton et al., 2007; Teis et al., 2008, 2010), which induces subunit turnover within ESCRT-III promoting either polymer disassembly (Adell et al., 2014; Yang et al., 2015) or growth (Mierzwa et al., 2017). ESCRT-III subunits assemble into single- or multiple-stranded filaments, which exhibit high spontaneous curvature and low rigidity, leading to diverse shapes from spirals (Chiaruttini et al., 2015; Hanson et al., 2008; Henne et al., 2012; Shen et al., 2014) to conical spirals (Hanson et al., 2008; McCullough et al., 2015) and tubular helices (Effantin et al., 2013; Lata et al., 2008). To date, the mechanism by which ESCRT-III polymers drive membrane remodeling remains unclear (Chiaruttini and Roux, 2017). However, many recent findings support the notion that ESCRT-III polymer remodeling by Vps4 is required (Adell et al., 2017; Guizetti et al., 2011; Mierzwa et al., 2017).

Attempts to reconstitute membrane fission *in vitro* using ESCRT-III core subunits have led to conflicting reports regarding the role of Vps4 (Schöneberg et al., 2018; Wollert et al., 2009). Polymers observed with these subunits (Snf7, Vps2, and Vps24) exceed radii of 15 nm (Henne et al., 2012; Lata et al.,
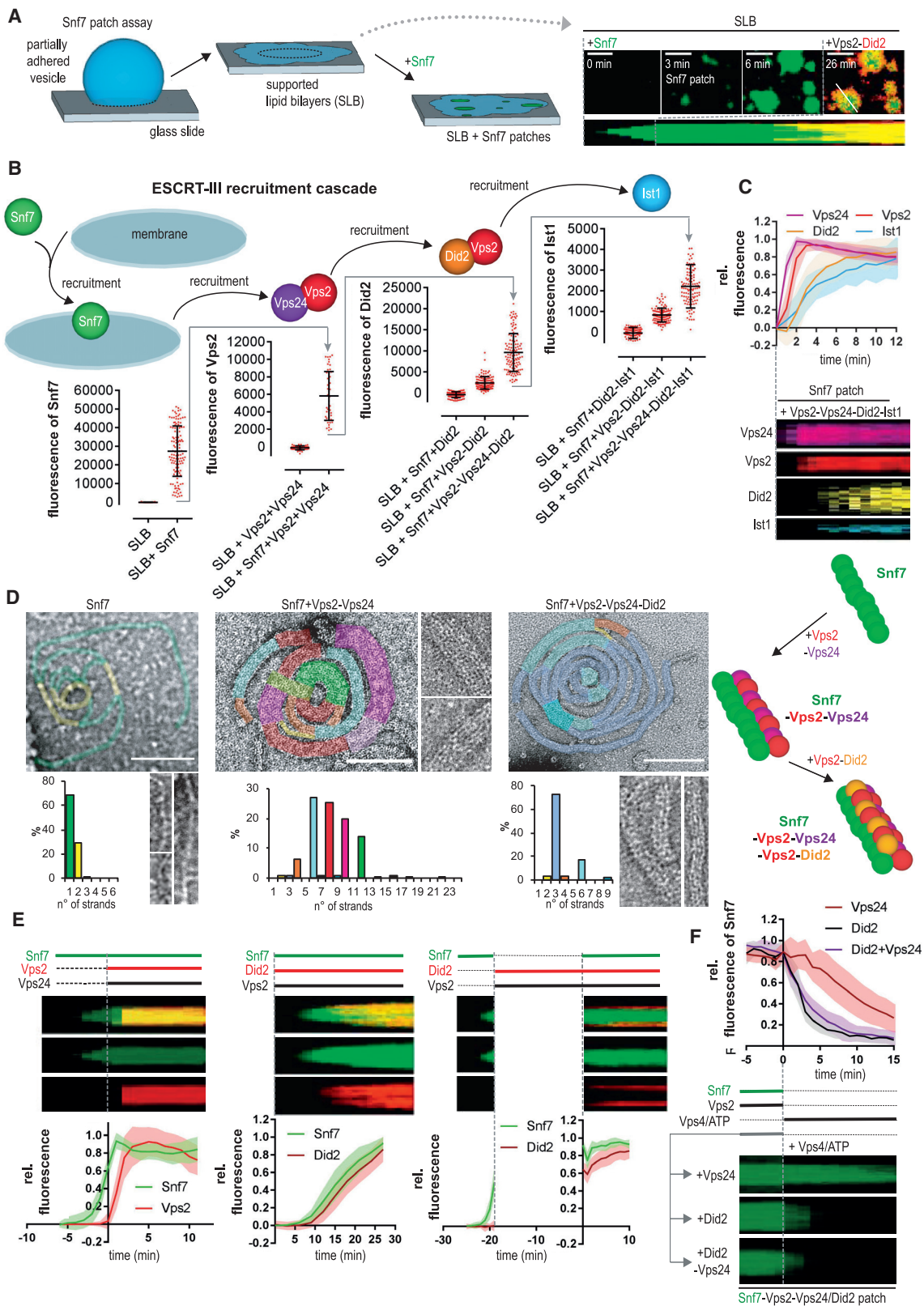
2008; Mierzwa et al., 2017; Shen et al., 2014). While further constriction can be achieved by the addition of Vps4 (Maity et al., 2019), these dimensions remain far from the theoretical limit of 3 nm required for spontaneous fission (Kozlovsky and Kozlov, 2002). This suggests that additional factors or mechanisms are at play in ESCRT-III-dependent membrane fission.

Aside from the core ESCRT-III proteins, accessory ESCRT-III proteins have been proposed to play roles in the context of specific ESCRT-III functions (Schöneberg et al., 2017). Two of these, CHMP1 and IST1, contribute to many ESCRT-dependent processes and have a strong loss-of-function abscission phenotype (Agromayor et al., 2009; Bajorek et al., 2009a, 2009b; Xiao et al., 2009). Likewise, a knockout of Did2 (yeast CHMP1 homolog) results in cargo sorting defects similar to those observed upon depletion of ESCRT-III core subunits (Brune et al., 2019; Nickerson et al., 2006; Talledge et al., 2018). CHMP1B-IST1 co-polymers also form the tightest ESCRT-III helices and are able to constrict membrane tubules (McCullough et al., 2015; Nguyen et al., 2020). These observations point to a more important, yet unrecognized, role of Did2/CHMP1 and Ist1/IST1 in ESCRT-III function.

RESULTS

ESCRT-III Subunits Undergo Cascade-like Recruitment

To study how ESCRT-III polymers recruit Did2 and Ist1, we incubated Alexa488-Snf7-patches grown on supported lipid bilayers (Chiaruttini et al., 2015; Figure 1A) with Atto565-Did2 or Atto565-Ist1 and varying combinations of ESCRT-III subunits at equimolar concentrations (Figures S1A–S1D). Like Vps2 and Vps24, which bind Snf7 as an obligatory dimer (Mierzwa et al., 2017), Did2 was co-recruited with Vps2 to Snf7-patches suggesting that Vps2 and Did2 form a novel Snf7-binding sub-complex, a notion supported by recent genetic studies (Brune et al., 2019; Heinzle et al., 2019). Did2-binding was, however, strongly enhanced by Vps24. Consistently with its known affinity for Did2, Ist1 recruitment mirrored that of Did2, in that it was recruited with Vps2-Did2 and bound most efficiently to Snf7-patches in the presence of Vps2-Vps24-Did2 (Figures S1C and S1D). Altogether, these findings indicate that ESCRT-III subunits are organized in a recruitment cascade: membrane-bound Snf7 recruits Vps2-Vps24, which recruits Vps2-Did2, which then recruits Ist1 (Figure 1B). This led us to wonder about the binding dynamics of the different subunits. Thus, we extracted kymographs of

each subunit from midsections of pre-grown Snf7-patches after simultaneous addition of all subunits (Figure 1C). Strikingly, the recruitment dynamics of the subunits followed the same order expected from our affinity study (Figure 1B).

Vps2 and Did2 Form an Snf7 Binding Complex

To better characterize Vps2-Did2, the most poorly described ESCRT-III sub-complex, we performed negative stain electron microscopy of Snf7-coated liposomes incubated with Vps2, Vps24, and Did2 (Figure 1D). As previously reported (Chiaruttini et al., 2015; Mierzwa et al., 2017), Snf7 formed single-stranded spirals, which upon addition of Vps2 and Vps24, transitioned into multimers of double-stranded spirals suggesting a lateral co-polymerization (see STAR Methods). Interestingly, the further addition of Vps2-Did2 resulted in the formation of three-stranded spirals indicating that Vps2-Did2 forms a third filament along Snf7-(Vps2-Vps24) filaments (Figure 1D). Strikingly, intertwined multi-stranded spiral-like polymers formed upon addition of Vps2-Did2 alone to Snf7-spirals demonstrating that Vps2-Did2 is sufficient to induce Snf7 filament bundling (Figure S1E).

To better understand how Did2-Vps2 and Vps24-Vps2 interact within ESCRT-III polymers, Snf7-patches were incubated with Vps2, Atto565-Did2, and increasing concentrations of Vps24. Consistent with the Vps24-mediated enhancement of Did2-Vps2 co-recruitment (Figures S1A and S1B), the Did2 binding rate and level of recruitment were the highest when Vps2, Vps24, and Did2 were added at stoichiometric ratios of 2:1:1 (Figures S1F and S1G). Conversely, higher concentrations of Vps24 reduced binding of Did2 to Snf7-patches. Because competitive binding between Vps24 and Did2 for Vps2 seems unlikely in a scenario where Vps24 also participates in Did2 recruitment, the inhibition of Did2-binding likely resulted from depletion of Vps2 from the soluble protein pool by binding to Vps24. Because formation of a Did2-homopolymer on top of pre-existing Snf7-(Vps2-Vps24) filaments should not be affected by depletion of free Vps2, the inhibition of Did2-binding upon Vps2-depletion strongly suggests that Did2 is recruited to ESCRT-III as Did2-Vps2 heterodimers. Because Snf7-Vps2-Vps24-Did2 forms three-stranded filaments, while Snf7 is sufficient to recruit Vps2-Did2, and Vps2-Vps24 enhances Did2 recruitment, we think that Vps2-Did2 forms a heteropolymer that interacts with both Snf7 and Vps2-Vps24 filaments (Figure 1D). We further speculate that the three strands observed in Snf7-Vps2-Vps24-Did2 spirals are formed by a sequential

---

Figure 1. ESCRT-III Subunits Undergo Cascade-like Recruitment

(A) Scheme of supported lipid bilayer (SLB) Snf7-patch assay (scale bar, 5 μm). Alexa488-Snf7 was added at t = 0 min, Atto565-Did2 and Vps2 were added at t = 6 min.

(B) Quantification of Alexa488-Snf7, Atto565-Vps2, Atto565-Did2, or Atto565-Ist1 fluorescence of Snf7-patches or SLB incubated with the indicated proteins (mean ± SD).

(C) Kymographs and fluorescence quantification of patch assays. Subunits were added at t = 0 min to pre-grown Snf7-patches. Fluorescence was measured over time (n ≥ 3; Vps2 region of interest [ROI] = 36, Vps24 ROI = 68, Did2 ROI = 85, Ist1 ROI = 60; mean ± SD).

(D) Negative stain electron micrographs of ESCRT-III filaments on large unilamellar vesicles (LUVs). Zoom-ins and histograms of the distribution of strands number (n°) (scale bar, 100 nm) and proposed assembly of Snf7-Vps2-Vps24-Did2 filaments.

(E) Kymographs and fluorescence quantification of Snf7-patch assays. ESCRT-III proteins were added at indicated time points (gray dash line) (Vps2: n = 3, ROI = 162; Did2: n = 3, ROI = 87; saturated Did2: n = 3, ROI = 93; mean ± SD).

(F) Kymographs and fluorescence quantification of patch assays with Vps4/ATP added at t = 0 min to pre-grown Alexa488-Snf7-patches pre-incubated with indicated proteins. Fluorescence was measured over time (Vps24: n = 3, ROI = 32; Did2: n = 4, ROI = 50; Vps24-Did2: n = 3, ROI = 40; mean ± SD).

See also Figure S1.

polymerization that is initiated by an Snf7 homo-filament, along which a Vps24-Vps2 hetero-filament copolymerizes, which then recruits Did2-Vps2 (Figure 1D). Consistent with this sequence, Did2 did not affect Vps2-Vps24 binding to Snf7 (Figure S1H).

Because Did2 appears to have similar interactions with ESCRT-III subunits as Vps24, we next compared the functional properties of Vps2-Did2 and Vps2-Vps24. First, we tested Vps2-Did2 for its ability to inhibit Snf7 polymerization, a well described feature of Vps2-Vps24 (Mierzwa et al., 2017; Teis et al., 2008). Although addition of Vps2-Vps24 arrested growing Snf7-patches, Snf7-patches still grew slowly in presence of Vps2-Did2 (Figure 1E). This partial inhibition of growth could arise because Vps2-Did2 is only a weak inhibitor of Snf7 polymerization, or because Vps2-Did2 has a relatively low affinity for Snf7 polymers (Figure 1C). To discriminate these two possibilities, Snf7-patches were saturated with Vps2-Did2 in absence of free Snf7, before free Snf7 was re-introduced. In this case, growth was fully inhibited (Figure 1E). The addition of Vps2-Vps24-Did2 inhibited growth as efficiently as Vps2-Vps24 (Figure S1I). These results indicate that Vps2-Did2, like Vps2-Vps24, can fully inhibit Snf7 polymerization. However, presumably because of its lower affinity for Snf7, Vps2-Did2 does not reach sufficient stoichiometry in the copolymer to fully inhibit Snf7 polymerization. Most likely, this partial inhibition of Snf7 polymerization by Vps2-Did2 explains the large variation in size and number of strands observed in Snf7-Vps2-Did2 spirals (Figure S1E). The second function of Vps2-Vps24 is to recruit Vps4, which promotes disassembly of ESCRT-III in absence of free Snf7. Interestingly, Vps2-Did2 promoted disassembly of Snf7-patches more efficiently than Vps2-Vps24 (Figure 1F). When both Vps24 and Did2 were present in equimolar amounts, Did2 dominated the disassembly dynamics (Figure 1F). These results show that Vps2-Vps24 and Vps2-Did2, although having seemingly redundant functions in ESCRT-III assembly, possess functional specializations, with Vps2-Vps24 having a stronger affinity for Snf7-polymers, whereas Vps2-Did2 stimulates Vps4 more efficiently.

Vps4 Exchanges Vps2-Vps24 for Vps2-Did2 within ESCRT-III Polymers

Because Vps2-Vps24 and Vps2-Did2 are sequentially recruited to Snf7-patches, we wondered if their disassembly also follows a fixed order. Thus, we monitored Vps24 and Did2 levels upon Vps4-triggered disassembly of Snf7-(Atto565-Did2)-(Alexa488-Vps24)-Vps2-patches. Interestingly, Vps24 promptly disassembled upon addition of Vps4/ATP, whereas Did2 intensity initially increased on Snf7-patches (Figure 2A) suggesting that Vps4 exchanges Vps24 for Did2 in Vps2 heteropolymers. To test this, the disassembly of Snf7-(Alexa488-Vps24)-(Atto565-Vps2)-patches was monitored in the presence and absence of Did2, and the ratio of Vps24 and Vps2 fluorescence intensities (Vps24/Vps2 ratio) was observed. Similar experiments were performed using Snf7-Vps24-(Alexa488-Vps2)-(Atto565-Did2)-patches to assess the Did2/Vps2 ratio. Intriguingly, the Vps24/Vps2 ratio decreased upon Vps4-induced subunit-turnover in presence of Did2, whereas it remained stable when Did2 was missing (Figure 2B). Conversely, the Did2/Vps2 ratio initially increased and then plateaued, implying that Vps24 is first

exchanged for Did2 (initial phase) (Figure 2B), before the Did2-Vps2 filament disassembled (plateau). Taken together, these findings reveal the exchange of subunits within a persistent ESCRT-III polymer that is driven by the different biochemical properties of the subunits themselves. Due to its stronger affinity for Snf7, Vps24-Vps2 is recruited first to Snf7-patches. Vps24 is then exchanged for Did2, which stimulates Vps4 activity to remove Snf7 while Vps2 remains stably bound at the membrane. These dynamics are in good agreement with data from yeast in which Vps24 and Snf7 accumulated in the did2Δ mutant (Nickerson et al., 2006).

Vps2-Vps24 versus Vps2-Did2—Should I Shrink or Should I Grow?

When recruited by Vps2-Vps24, Vps4 induces subunit-turnover driving the growth of Snf7-patches in presence of free Snf7 (Mierzwa et al., 2017). By contrast, the recruitment of Vps4 by Vps2-Did2 promotes the disassembly of Snf7-patches (Figure 2C). These findings indicate that Vps2-Vps24 and Vps2-Did2 have opposing effects on the growth and disassembly of Snf7-polymers. Because the ratio between Vps24 and Did2 in ESCRT-III assemblies changes over time (Figures 1C and 2B), we asked if the overall growth or depolymerization rate was controlled by the Vps24/Did2 molar ratio. To address this issue, we monitored the outcome (growth or disassembly) of Alex488-Snf7-Vps2-patches incubated with varying ratios of Vps24/Did2 upon addition of Vps4/ATP. Thrillingly, Snf7 turnover dynamics could be shifted from growth to disassembly by decreasing the Vps24/Did2 ratio in presence of free Snf7 (Figure 2D). We envision that a growing Snf7-polymer first recruits Vps2-Vps24 due to it higher affinity. Vps2-Vps24 then recruits Vps4, which upon low stimulation promotes polymer growth and exchanges Vps24 for Did2. Increasing levels of Did2 slowly recruit and stimulate Vps4 so that, once the Vps24/Did2 ratio falls below a critical value, highly active Vps4 triggers the disassembly of Snf7-polymers.

Sequential Disassembly of ESCRT-III Subunits

The demonstration that the Vps24/Did2 ratio controls the growth dynamics of ESCRT-III assemblies suggests a sequential pathway of polymer disassembly (Figure 2). To monitor the Vps4-mediated disassembly dynamics of individual subunits within multi-subunit ESCRT-III assemblies, we added Vps4/ATP to Snf7-patches pre-incubated with saturating levels of Vps2-Vps24-Did2-Ist1 (Figure 3A), while maintaining the soluble pool of all subunits. Interestingly, subunits disassembled sequentially: Snf7 and Vps24 depolymerized rapidly, Vps2 disassembled with a delay, while Did2 and Ist1 remain stably bound to the assemblies. The delay in Vps2-disassembly was dependent on Did2 (Figure 3B) and is most likely mediated by the formation of a stabilizing Vps2-Did2 complex upon exchange of Vps24 with Did2 (Figure 2B). Furthermore, Did2 depolymerized in absence of soluble Ist1 but remained at the patches when Ist1 was present (Figure S1J). To further study this process, we switched colors of soluble pools of Did2 or Ist1 before addition of Vps4/ATP by replacing Atto488-labeled with Atto565-labeled Did2 or Ist1 (Figure 3C). Although Ist1 continuously exchanged with its soluble pool, Did2 did not. Previous structural studies
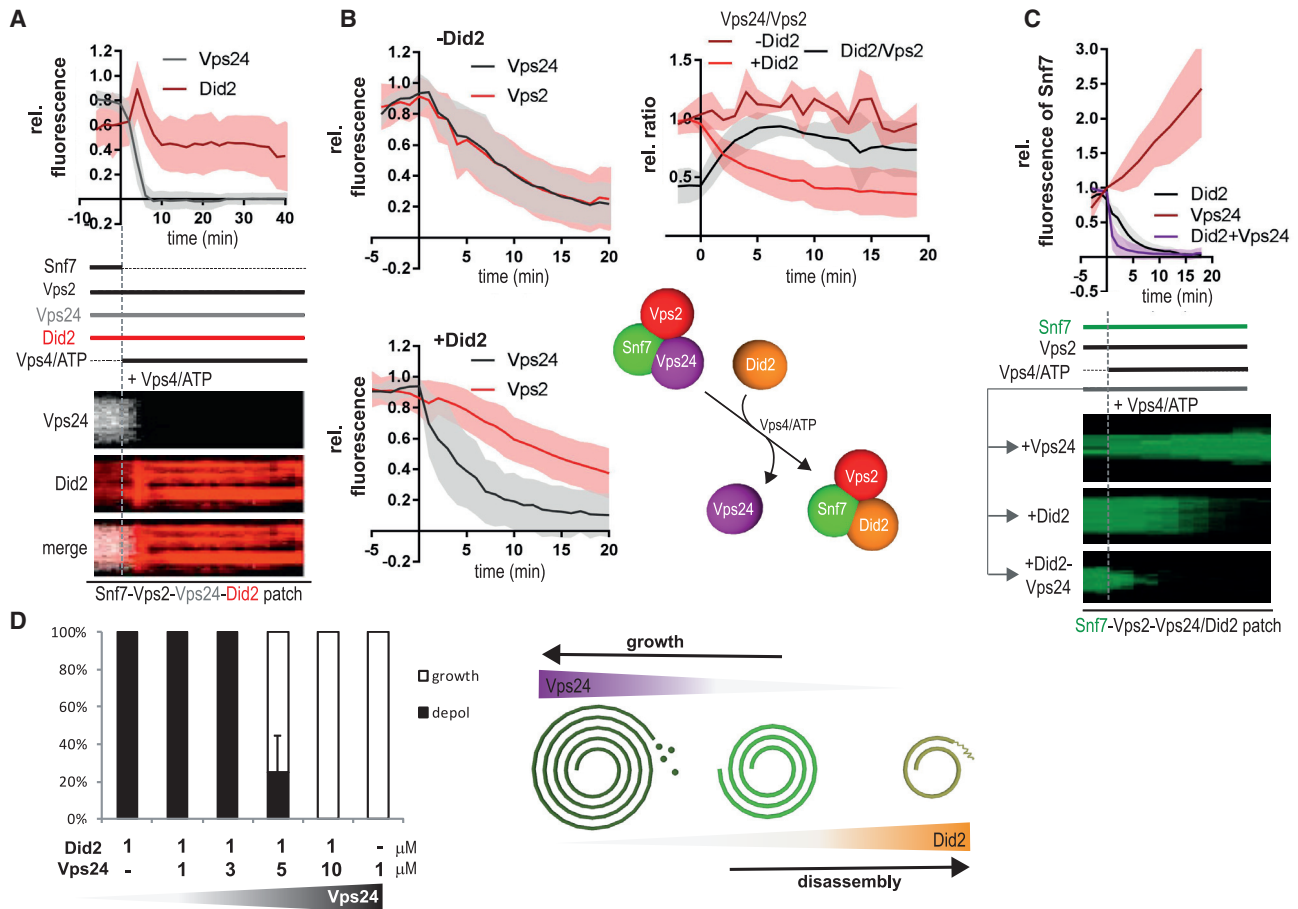
Figure 2. Vps4 Exchanges Vps2-Vps24 for Vps2-Did2 within ESCRT-III Polymers

(A–C) Kymographs and fluorescence quantification of patch assay. Vps4/ATP was added at t = 0 min to pre-grown Snf7-patches pre-incubated with indicated proteins. Fluorescence was plotted against time.

(A) n = 3, ROI = 43; mean ± SD.

(B) −Did2: n = 4, ROI = 49; +Did2: n = 4, ROI = 95; mean ± SD (left panels). Fluorescence ratios of Vps24/Vps2 or Did2/Vps2 plotted over time (Vps24/Vps2: n = 4; Did2/Vps2: n = 3; mean ± SD) (right top panel). Schematic representation of Vps4-triggered exchange of Vps24 to Did2 (right bottom panel).

(C) Vps24: n = 3, ROI = 88; Did2: n = 3, ROI = 143; Vps24-Did2: n = 3, ROI = 142; mean ± SD.

(D) Percentage of growing versus depolymerizing (depol) Snf7-patches as a function of Vps24 and Did2 concentrations (n ≥ 3; mean ± SD).

See also Figure S1.

suggested that, due to steric hindrance, CHMP1B (mammalian Did2 homolog) binds either IST1 or Spastin, an ATPase similar to Vps4 (Obita et al., 2007; Stuchell-Brereton et al., 2007; Talledge et al., 2018; Xiao et al., 2009). This led to the idea that Ist1 could prevent Did2 disassembly by masking its Vps4 binding-site. Consistently, Did2 disassembly could be induced by decreasing the Ist1/Vps4 molar ratio (Figure 3C), demonstrating that Ist1 binding competes with Vps4-triggered Did2 disassembly. In this way, Ist1 protects Did2 from depolymerization. In summary, our results indicate that a cascade of subunit recruitment is followed by a Vps4-driven sequential polymer disassembly. This suggests the possibility that ESCRT-III function is based on a specific sequence of subunit recruitment and exchange. To test this hypothesis, we set out to reconstitute this assembly sequence *in vitro*.

Vps4 Drives a Polymerization Sequence of ESCRT-III Subunits

To provide a nucleation platform for all subunits, we grew Snf7-patches to which Snf7-Vps24-Vps2-Did2-Ist1-Vps4/ATP were added in a molar ratio of 2:1:0.8:1.5:1:1.5 respectively, resembling the experimentally estimated abundance of ESCRT-III subunits (1.7:1:N/A:1.3:2.5:2.8 [Ghaemmaghami et al., 2003] and 2.5:1:1:N/A:N/A:N/A [Teis et al., 2008]; Figures 4A and S2A). For the analysis of subunit dynamics, we imaged Alexa488-Snf7 with one Atto565-labeled subunit and then normalized the sequence using Snf7 dynamics as reference (Figure S2A; STAR Methods). Alexa488-Ist1 was normalized against Atto565-Vps2 for technical reasons.

Immediately after addition of all subunits, Snf7-patches started to grow, accompanied by strong Vps24 recruitment to
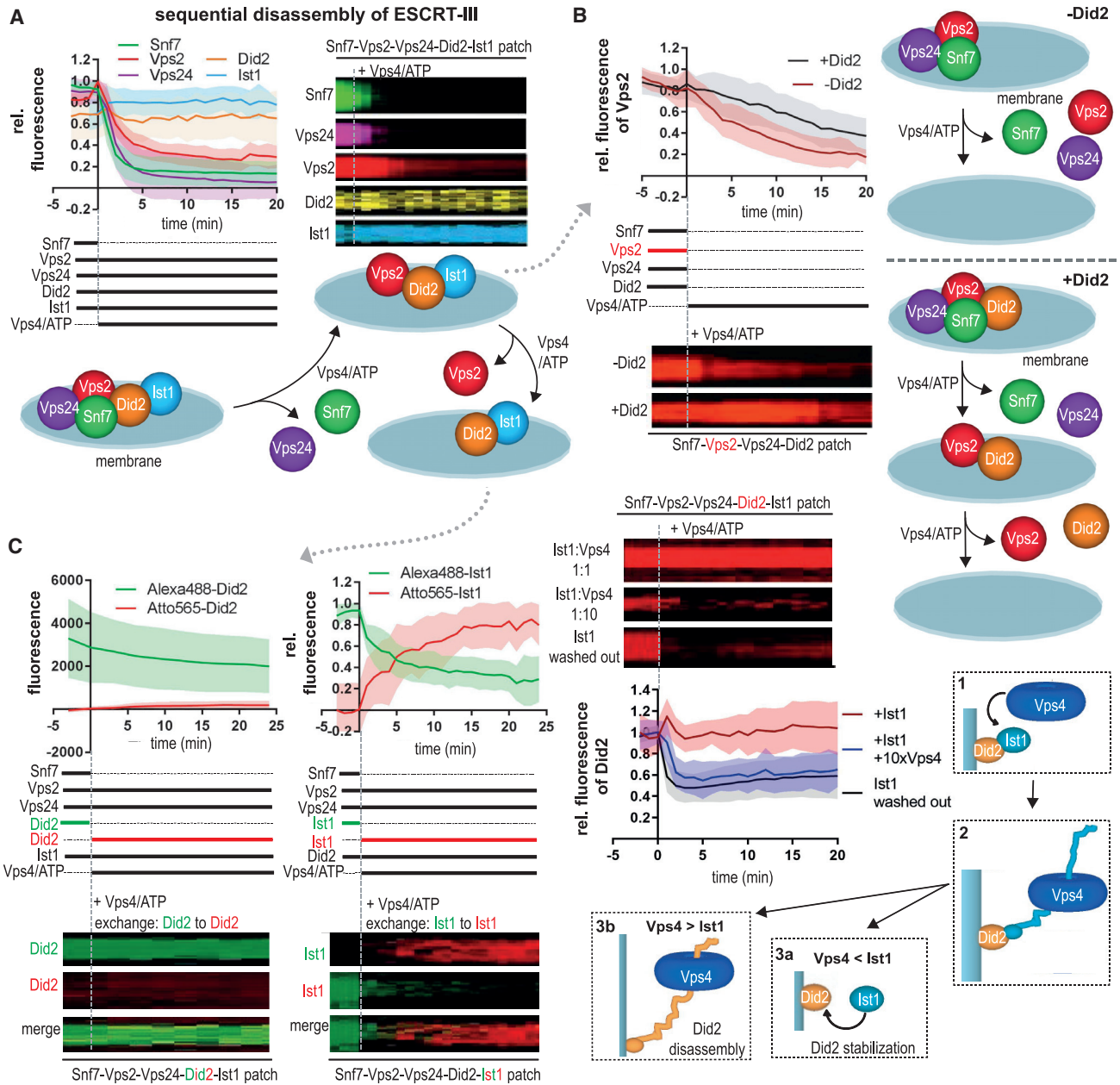
Figure 3. Vps4 Triggers Sequential Disassembly of ESCRT-III Subunits

(A–C) Kymographs and fluorescence quantification of patch assays. Vps4/ATP was added at t = 0 min to pre-grown Snf7-patches pre-incubated with indicated proteins. Fluorescence was plotted against time (see STAR Methods for details).

(A) Snf7: n = 3, ROI = 72; Vps2: n = 3, ROI = 97; Vps24: n = 3, ROI = 110; Did2: n = 4, ROI = 109; Ist1: n = 4, ROI = 129; mean ± SD.

(B) −Did2: n = 4, ROI = 67; +Did2: n = 3, ROI = 127; mean ± SD.

(C) Before addition of Vps4, the soluble pool of Alexa488-Did2/Ist1 was exchanged for Atto565-Did2/Ist1 (n = 3; Did2: ROI = 54 (left panel); Ist1: ROI = 46 (middle panel; mean ± SD). 10xVps4 corresponds to a condition where Vps4 concentration was increased ten times. −Ist1: n = 3, ROI = 188; 10xVps4: n = 3, ROI = 76; washed out: n = 3 ROI = 55; mean ± SD) (right panel).

See also Figure S1.

patches, but only a modest accumulation of Vps2, Did2, and Ist1. Shortly thereafter, Vps24 fluorescence rapidly dropped, Snf7-patches started to disassemble, while Vps2-accumulation peaked and levels of Did2 and Ist1 increased. Then, Vps2 disas-

sembled, while Did2 and Ist1 fluorescence continued to increase before dropping gradually. These results demonstrate that ESCRT-III is a dynamic polymer that, after nucleation, spontaneously undergoes a Vps4-driven sequence of assembly and
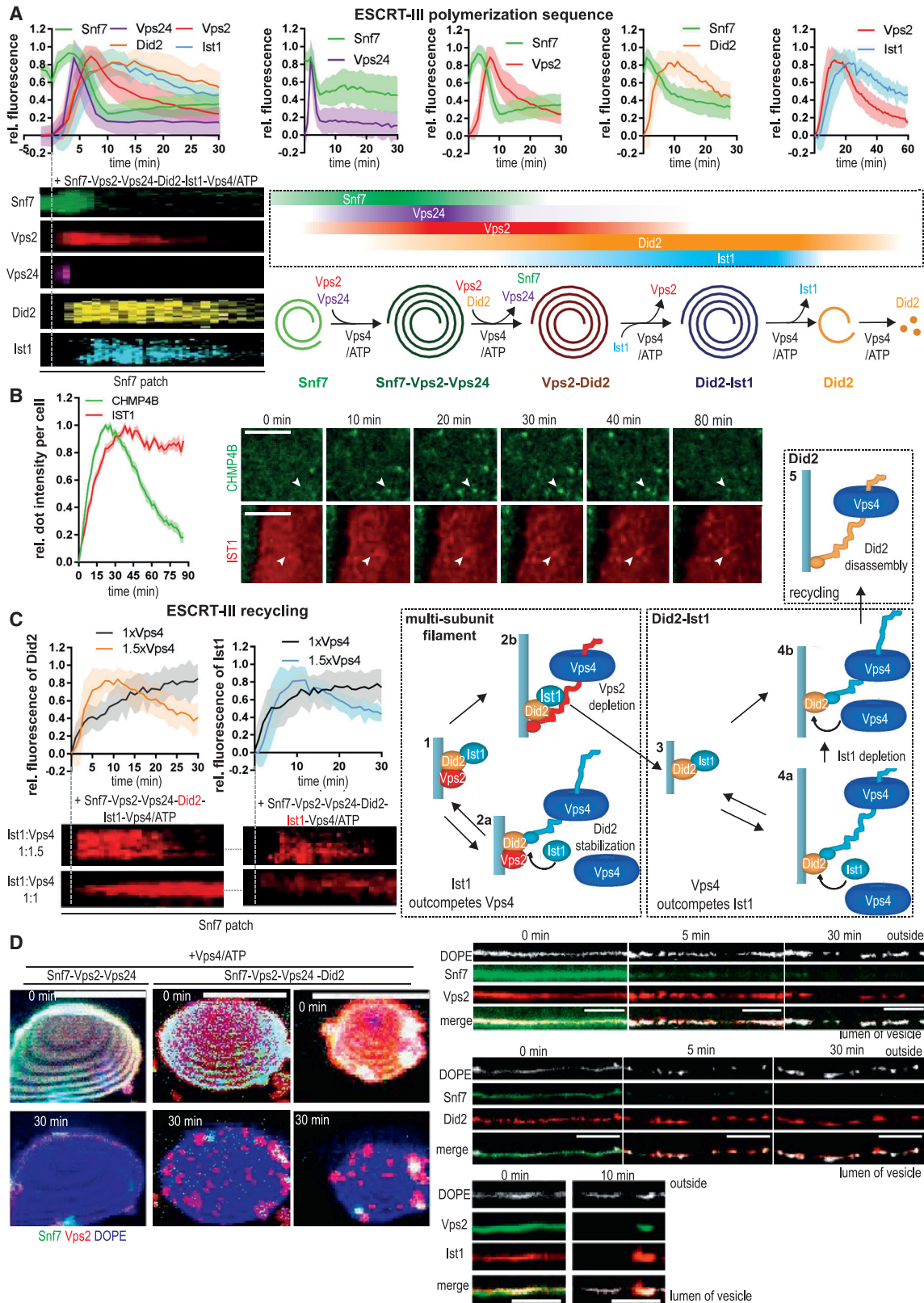
disassembly whose order is determined by the different biochemical properties of its subunits. We find that the initial Snf7 structure primarily recruit Vps2-Vps24, because of its high affinity for Snf7. Vps2-Vps24, in turn, recruits Vps4, which promotes filament growth upon low stimulation via Vps2-Vps24. As increasing levels of Did2 further stimulate Vps4 activity, highly sensitive Snf7 and Vps24 filaments then disassemble rapidly, while Vps2 depolymerizes with a delay and Did2, protected from disassembly by Ist1, accumulates. Importantly, these sequential changes in filament composition all occur in the presence of a soluble pool of free subunits, indicating that the observed assembly and disassembly are unidirectional.

The ESCRT-III recruitment sequence we describe here has never been observed before, probably because Did2 and Ist1, which step in later in the sequence than Vps2, Vps24, and Snf7, were omitted from similar experiments (Adell et al., 2017; Bleck et al., 2014). When ESCRT-III recruitment to endosomes was triggered by hypertonic shock in mammalian cells (Mercier et al., 2019), we observed a delayed recruitment of IST1 relative to CHMP4B (Snf7 homolog) (Figures 4B and S2B), indicating that a similar sequence of ESCRT-III recruitment events occurs *in vivo* during triggered ESCRT-III activity. *In vitro*, one cycle of ESCRT-III assembly and disassembly took several minutes, which is longer than ILVs formation or viral budding but shorter than abscission (Adell et al., 2017; Bleck et al., 2014; Christ et al., 2016; Guizetti et al., 2011; Johnson et al., 2018). Because membrane curvature in our supported bilayer assay and at the cytokinetic bridge is much smaller than that found at the neck of ILV buds, we speculate that membrane curvature could influence the kinetics of subunit recruitment and turnover.

Interestingly, when Ist1 and Vps4 were present in equal amounts *in vitro*, Ist1 and Did2 saturated at the membrane, while disassembly occurred when more Vps4 was added (Figure 4C). This implies that changing the balance between Ist1-dependent Did2-stabilization and Vps4-induced Did2-disassembly during the polymerization sequence could allow, first, the formation of Did2-Ist1 polymers, followed by their subsequent disassembly. When Vps4 targets besides Did2 and Ist1 are present (e.g., Vps2), Ist1-mediated Did2-protection outcompetes Vps4, resulting in the depletion of Vps2 while Did2 remains on the membrane. It is only when Did2-Ist1 are alone that Vps4 can overcome Ist1-mediated Did2-protection to promote Did2 disassembly. Similarly, following recruitment *in vivo*, IST1 remained on endosomes, whereas CHMP4B was disassembled (Figure 4B), as was seen *in vitro* in the presence of low Vps4/Ist1 ratios. We speculate that global ESCRT-III recruitment might

diminish the cytosolic pool of Vps4 and thereby inhibit disassembly of IST1. Taken together, these data indicate recycling of ESCRT-III after membrane fission might occur via a shift in polymer composition that changes the outcome of competitive binding between Ist1 and Vps4.

Sequential Polymerization of ESCRT-III Drives Membrane Deformation

Upon Vps4-induced disassembly of ESCRT-III polymers on deformable membrane, we observed formation of bright puncta accumulating Atto565-Vps2, Atto565-Did2, Atto565-Ist1, the membrane marker Atto647N-dioleoylphosphatidyl ethanolamine (DOPE), and temporarily, Alexa488-Snf7 (Figure 4D). Because this accumulation of Atto647N-DOPE puncta could represent local membrane deformation, we analyzed liposomes coated with various ESCRT-III subunits by negative-stain and freeze-fracture electron microscopy. Incubation with Snf7 alone, Snf7-Vps2-Vps24, or Snf7-Vps2-Vps24-Vps4/ATP yielded flat spiral-filaments (Figures 5A and S3A). The addition of Did2 resulted in a moderate 3D-deformation of spiral-filaments (diameter, 31.5 nm ± 6.8 nm) (Figure 5A) and modest membrane deformations (diameter, 53 nm ± 12.8nm) (Figure 5A). Supplementing the mixture with Vps4/ATP, caused massive 3D-deformations of filaments, characterized by tubular structures protruding from the spiral center (diameter, 16.3 nm ± 3.5 nm) (Figure 5A). The corresponding membrane deformations frequently extended deep inside vesicles, eventually breaking during the fracturing procedure. Consistently, negative stain of the inner leaf flat of burst vesicles revealed membrane protrusions expanding toward the inside of vesicles (22.1 nm ± 3.2 nm) (Figure 5A). We presume that these membrane protrusions are formed by the observed protein filaments and two layers of membrane bilayers (ca. 4 nm each). Altogether, we show that Did2 incorporation into ESCRT-III filaments promotes their 3D-deformation, which triggers formation of inward-directed membrane protrusions. Because Vps4 promotes efficient disassembly of Snf7 and Vps24 from polymers, whereas Vps2-Did2 structures remain, this boost in membrane deformation by Vps4 is likely due to a shift in polymer composition.

A recent computational model, in which driven sequential changes in the polymer orientation relative to the membrane caused flat spirals to transition into conical and helical polymers, could explain how a shift in polymer properties imposed by changes in its composition might drive filament deformation (Harker-Kirschneck et al., 2019). Consistently, cryoelectron microscopy (cryo-EM) of Snf7-Vps2-Vps24 and Snf7-Vps2-Did2
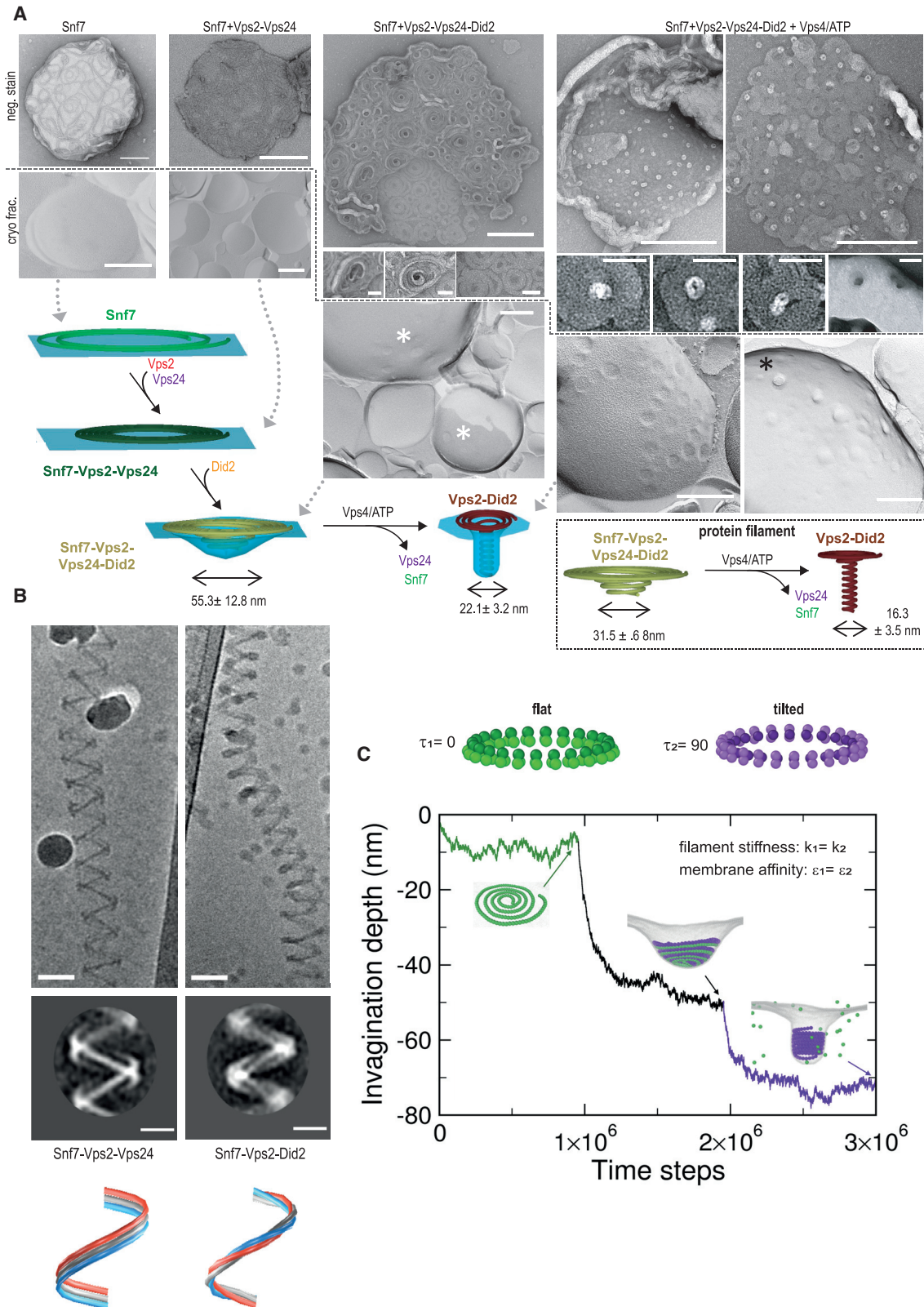
Figure 4. Vps4 Drives a Polymerization Sequence of ESCRT-III Subunits

(A) Kymographs and fluorescence quantification of patch assays and model of sequential ESCRT-III recruitment. Indicated proteins were added to pre-grown Alexa488-Snf7 patches at t = 0 min. Fluorescence intensities of Alexa488-Snf7 and Atto565-labeled protein (n = 3; Vps2: ROI = 108; Vps24: ROI = 65; Did2: ROI = 55; mean ± SD), and Atto565Vps2 and Alexa488-Ist1 (n = 4 ROI = 71; mean ± SD) were monitored and plotted against time (left panel, scaled graphs, see Figures S2A and S2I).

(B) Fluorescence quantification and images of life-cell imaging of endosomal recruitment of CHMP4B-GFP and IST1-mcherry after hypertonic shock (HS). HS was applied at t = 0 min. Arrows indicate one recruitment site over time (scale bar, 5 μm; CHMP4B: n = 3, ROI = 37; IST1: n = 3, ROI = 43; mean ± SEM).

(C) Kymographs and fluorescence quantification of patch assays in which indicated proteins and concentrations of Vps4 were added to pre-grown Snf7 patches at t = 0 min. Fluorescence was plotted over time (Did2:1.5xVps4: n = 3, ROI = 55; 1xVps4: n = 3, ROI = 41; Ist1:1.5xVps4: n = 4, ROI = 71; 1xVps4: n = 3, ROI = 47; mean ± SD). Schematic representation of interpretation.

(D) Vps4/ATP was added at t = 0 min to vesicles labeled with DOPE-Atto647N and pre-incubated indicated proteins. Tilted 3D projections of z stacks of partially adhered GUVs (left panel; scale bar, 10 μm) and linearized contours of GUVs (right panel; scale bar, 5 μm).

A

Snf7 | Snf7+Vps2-Vps24 | Snf7+Vps2-Vps24-Did2 | Snf7+Vps2-Vps24-Did2 + Vps4/ATP

B

C

(legend on next page)

filaments on lipid bicelles revealed that although both filaments appeared as double-stranded helices, Snf7-Vps2-Vps24 filaments formed ribbon-like filaments (Moser von Filseck et al., 2020) in marked contrast to Snf7-Vps2-Did2 filaments that appeared as twisted around their main axis (Figure 5B). This observed twist in the helical structure corresponds to the tilt of each subunit imposed in the simulations. We therefore extended the earlier model (Harker-Kirschneck et al., 2019) to include staged assembly/disassembly of multiple filaments as observed in our experiments (Figure 5A). First, we modeled the recruitment of tilted (helical) Vps2-Did2 polymers to the flat membrane-bound spirals (Snf7-Vps2-Vps24) before simulating removal of the flat filament. Note that for these simulations, we chose to use two-stranded filaments to mimic the initial recruitment of Vps2-Vps24, and the subsequent Vps4-dependent switch to Vps2-Did2 within ESCRT-III assemblies.

Strikingly, the binding of a helical filament to a flat spiral filament resulted in the formation of conical structures (Figure 5C). Upon disassembly of the flat filament, we then observed a rapid transition from a conical to an extended helical filament. As observed in our experiments, these changes in filament organization were associated with deformation of the underlying membrane first into shallow membrane dimple upon the recruitment of the second polymer, and then tubular membrane protrusion upon removal of the first filament (Figures 5A and 5C). Interestingly, membrane deformation by the conical copolymers depended on the relative stiffness and membrane affinity of the two filaments. Although filaments with equivalent mechanical properties induced a clear membrane deformation, the deformation was less pronounced if the second filament was less stiff than the first one (Figure S4A). Reduction of the membrane affinity of the second filament further decreased the membrane invagination depth (Figure S4A). In summary, these results combining dynamic, structural, and simulation approaches strongly indicate that, by inducing the sequential assembly and disassembly of two polymer strands with orthogonal membrane-binding interfaces, flat ESCRT-III spirals can transition into first conical spirals (filament recruitment) before buckling into helical polymers (filament removal) accompanied by membrane deformation into first shallow membrane dimples and then deeper membrane invaginations.

Ist1 Binding Promotes Membrane Constriction and Fission

Next, we examined the role of Ist1 by incubating Did2-mediated inward protrusions with Ist1. Strikingly, protrusions constricted from 22.1 nm ± 3.2 nm (Figure 5A) without Ist1 to 12.1 nm ±

1.8 nm when Ist1 was present (Figures 6A and S3B). To further characterize this constriction, we used membrane-bound Vps2-Did2 copolymers, which form outward tubular structures with a pearled appearance and helical collars. The diameter of these collars (20.1 nm ± 2 nm) (Figures 6B, 6C, and S3C) were comparable to the inward membrane protrusions (Figure 5A). When both, Ist1 and Vps4/ATP, were added in solution, the collars appeared to constrict in between bulges (13.5 nm ± 3.5 nm) with a spread distribution of diameters as expected for filaments undergoing a gradual asynchronous constriction. Based on our previous observations, Vps4 most likely depletes Vps2 from the ESCRT-polymer thereby establishing a tighter Did2-Ist1-polymer, fully consistent with a recent report of IST1-driven constriction of CHMP1B-polymers and the underlying membrane by structural subunit elongation (Nguyen et al., 2020).

Intriguingly, when membrane tubes were pre-absorbed onto EM grids before Vps4/ATP-treatment, Vps4-triggered polymer constriction led to tubule scission, as revealed by rows of aligned vesicles (Figures 6D and 6E). This suggests a role for tension in ESCRT-III-mediated fission, similar to dynamin-mediated fission (Danino et al., 2004; Morlot et al., 2012; Roux et al., 2006). To further test the fission efficiency of the Did2-Ist1 complex, we separated liposomes and small vesicles formed during ESCRT-III action by centrifugation, an assay previously used to test membrane fission by amphipathic helices (Boucrot et al., 2012). Only when liposomes were treated with Vps2-Did2-Ist1-Vps4/ATP small vesicles accumulated in the supernatant (Figures 6F and S3D) substantiating the notion that Ist1-induced constriction leads to fission. A caveat of these experiments, however, is that ESCRT-III-mediated fission occurs in the reverse orientation relative to most instances of ESCRT-III function *in vivo*, where subunits are found within the membrane neck. Thus, we set out to develop an assay that would enable us to investigate ESCRT-III-mediated fission with the reverse orientation.

ESCRT-III Polymerization Sequence Can Fission Membrane Necks *In Vitro*

A powerful assay to test recruitment of protein as a function of positive and negative curvature is pulling membrane tubes from giant unilamellar vesicles (GUVs) (Simunovic et al., 2017). In this assay, streptavidin-coated beads are put in contact with an immobilized GUV containing exposed biotin moieties, and a tube is pulled by moving the bead trapped in optical tweezers. Tubes can be pulled outward the GUV, or inward the GUV (Dasgupta and Dimova, 2014). In the latter case, glass beads are nearly completely engulfed by the GUV membrane, because of

---

Figure 5. Sequential Polymerization of ESCRT-III Drives Membrane Deformation

(A) Negative stained micrographs of LUVs (neg. stain; upper panel) or micrographs of freeze-fractured LUVs (cryo frac.; lower panel) incubated with the indicated proteins (scale bar, 200 nm; zoom: scale bar, 50 nm; white asterisk, Did2-induced deformations; black asterisk, fractured Did2-induced deformations). Schematic representation of shape and sizes of filaments (Snf7-Vps2-Vps24-Did2: ROI = 84; Snf7-Vps2-Vps24-Did2 + Vps4/ATP: ROI = 111; mean ± SD) and membrane structures(Snf7-Vps2-Vps24-Did2: ROI = 65; Snf7-Vps2-Vps24-Did2 + Vps4/ATP: ROI = 54; mean ± SD).

(B) Cryo-electro micrographs and 2D class averages of Snf7-Vps2-Vps24 and Snf7-Vps2-Did2 filaments on membrane bicelles (scale bar, 50 nm; zoom, 25 nm). Scheme of observed structures.

(C) Membrane invagination depth estimated by molecular dynamics simulation of sequential assembly and disassembly of two filaments with different filament tilts with respect to the membrane surface ($\tau_1 = 0$, flat, $\tau_2 = 90$, tilted). The geometry of one filament turn is shown above the graph with the membrane-binding faces depicted in lighter colors.
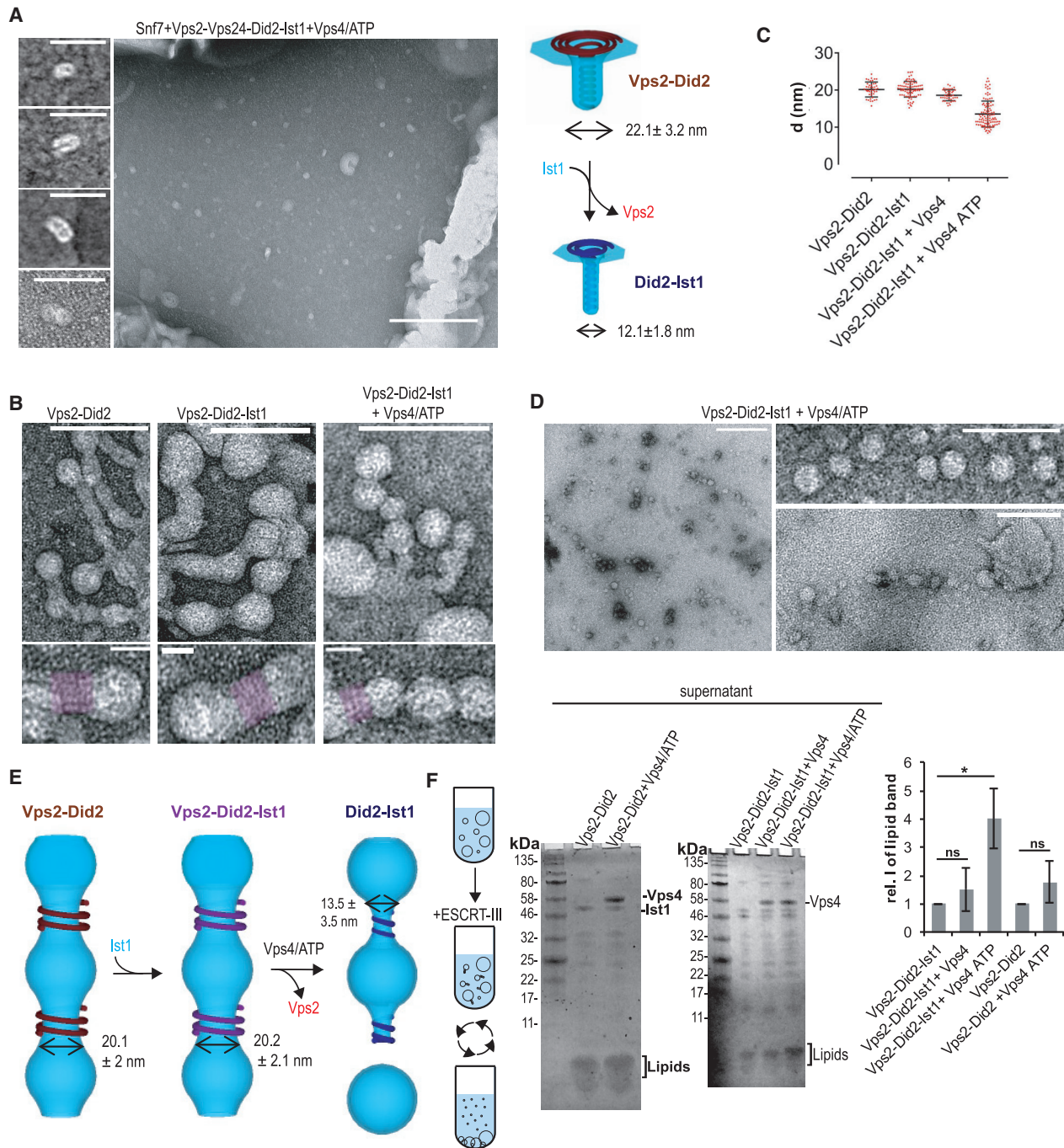
See also Figures S3 and S4.

Figure 6. Ist1 Binding Promotes Membrane Constriction and Fission

(A and B) Negative stained micrographs of LUVs incubated with indicated proteins and schematic representation of the observed structures. (A) Scale bar, 200 nm; zoom scale bar, 30 nm; −Ist1: ROI = 54; +Ist1: ROI = 76; mean ± SD. (B) Scale bar, 100 nm; lower panel: scale bar, 20 nm. Filament strands are indicated by overlaid purple color.

(C) Quantification of diameters of the helical structures (n = 3; mean ± SD).

(D) Negative-stained micrographs of LUVs pre-incubated with Vps2, Did2, and Ist1 and pre-absorbed on EM grids before Vps4/ATP was added (scale bar, 1.5 μm; zoom scale bar, 100 nm).

(E) Schematic interpretation of the structures observed in (B)–(D) with average radii (mean ± SD).

(F) Coomassie-staining of SDS-PAGE loaded with the supernatant after ultra-centrifugation of LUVs incubated with the indicated proteins. Quantification of lipid-bands intensity (n = 4; mean ± SD, t test, *p value < 0.05).
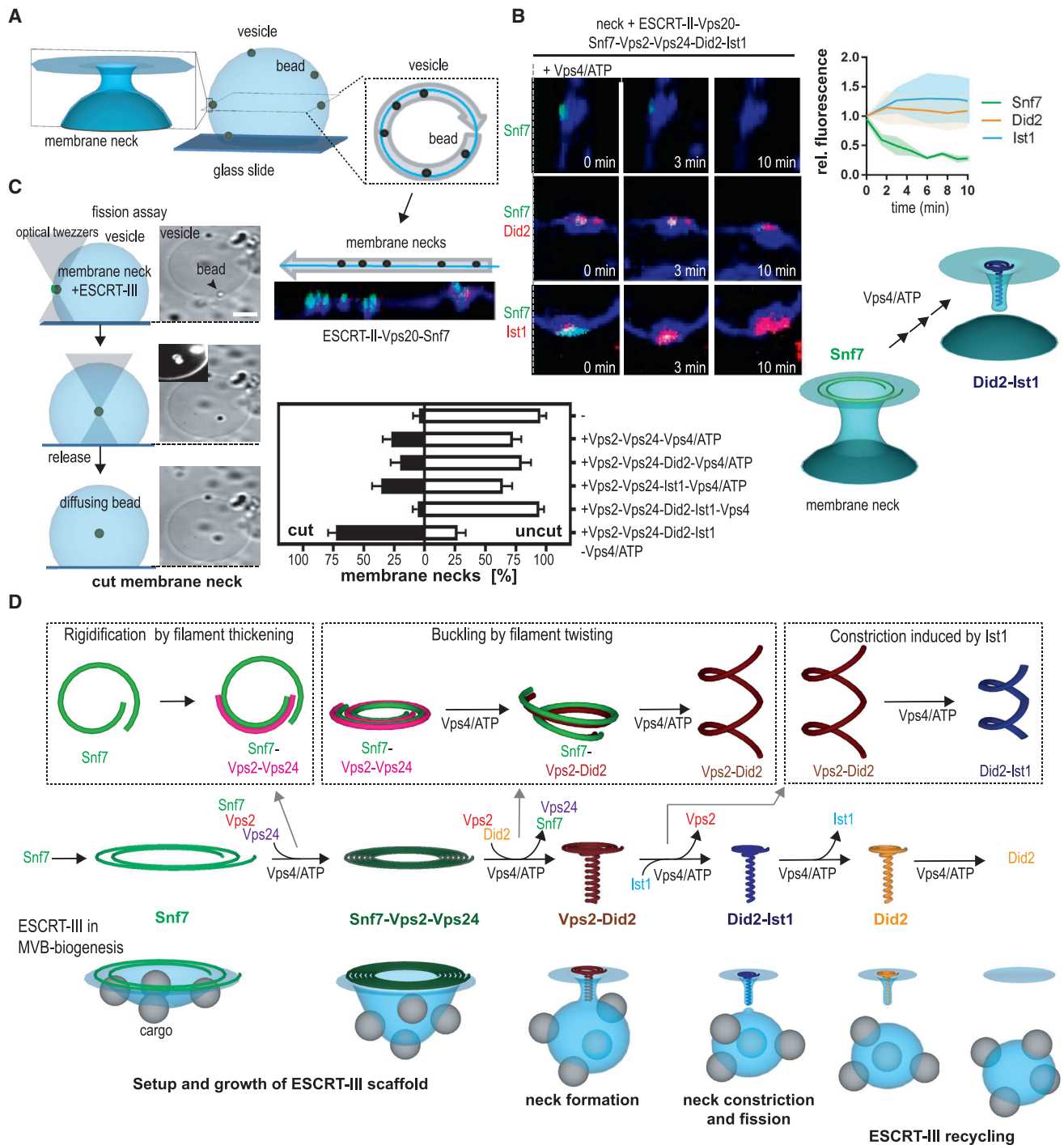
See also Figure S3.

Figure 7. ESCRT-III Polymerization Sequence Can Fission Membrane Necks *In Vitro*

(A) Schematic representation of artificial membrane necks assay with beads engulfed in GUVs and linearized contour of GUVs of membrane necks incubated with the indicated proteins.

(B) Confocal images and fluorescence quantification of artificial membrane necks incubated with the indicated proteins. Fluorescence was measured over time (Snf7: n = 3, ROI = 5; Did2: n = 3, ROI = 20; Ist1: n = 3, ROI = 23; mean ± SD).

(C) Schematic representation of the membrane fission assay and its discriminating criteria (see also Figure S6F). The indicated protein mixture was added to artificial ESCRT-II-Vps20-Snf7 membrane necks before pulling beads inside the GUVs and then releasing the beads (scale bar, 5 μm). – n = 5, ROI = 52;

(legend continued on next page)

the adhesive forces between glass and lipids. As reported previously, Snf7 did not polymerize on tubes pulled outward with a radius smaller than 35 nm (Figure S5A; Chiaruttini et al., 2015). Unexpectedly, Snf7 was also unable to bind to tubes pulled inward below a threshold radius of 115 nm (Figure S5A). The addition of ESCRT-II and Vps20, which were previously suggested to trigger the binding of Vps32 (*C. elegans* Snf7 homolog) or CHMP4B (human Snf7 homolog) to curved membranes (Fyfe et al., 2011; Lee et al., 2015), partially restored binding on positively curved tubes smaller than 35 nm as large Snf7 structures formed, but had no effect on binding of Snf7 to negatively curved tubes. We reasoned that the unidirectional curvature of tubes might prevent Snf7 binding. Necks have a prototypical saddle-like structure, in which both positive and negative curvatures come into play. To reproduce this saddle-like membrane architecture, instead of pulling engulfed glass beads into GUVs to form membrane tubes, we added ESCRT-III subunits to necks connecting engulfed beads to GUV membranes. At these necks, ESCRT-III nucleators ESCRT-II and Vps20 triggered site-specific nucleation of Snf7-structures (Figures 7A and S5C). These findings suggest that a curvature-sensitive nucleation and a curvature-sensitive inhibition of Snf7-polymer growth could help position polymerization of ESCRT-III polymers within neck structures.

To test if the ESCRT-III polymerization sequence we discovered on flat supported bilayers also occurs at these neck structures, we added mixtures of Vps2-Vps24-Did2-Ist1-Vps4/ATP to pre-grown ESCRT-II-Vps20-Snf7 necks. As expected, Vps2, Did2, and Ist1 were recruited, and we observed disassembly of Snf7, while Did2 and Ist1 remained at membrane necks upon Vps4/ATP-induced subunit-turnover (Figures 7B and S6A–S6E). We next tested if the ESCRT-III polymerization sequence can trigger fission of these membrane necks. To do so, engulfed beads with pre-grown Snf7 necks were incubated with various mixtures of ESCRT-III subunits before beads were pulled inside the vesicle using optical tweezers (Figures 7C and S6F). Beads that instantly retracted to the membrane when released because of a membrane tube, and beads that could not be pulled in, were both scored as non-fission events. Only beads that, after being pulled and released, remained in the GUV center were scored as fission events. In this regard, it should be noted that in previous attempts to monitor ESCRT-III-mediated fission based on outward tube pulling, tube detachment due to rupture of the DOPE-biotin-streptavidin association could erroneously be confused with membrane fission (Schöneberg et al., 2018). In contrast, in our assay, internalization of beads into the GUV signified by free diffusion of beads wrapped in fluorescent membrane could only occur by fission of the membrane neck. ESCRT-II and Vps20 were required in these experiments for the site-specific nucleation of Snf7-polymers at the neck structures (Figure S5C).

In absence of all ESCRT-subunits, 95.2% of the beads did not undergo fission. In contrast, fission occurred with 27.5%

efficiency when ESCRT-II-Vps20-Snf7-Vps2-Vps24-Vps4/ATP was added. Strikingly, the fission efficiency was dramatically increased, up to 72.8%, when both Did2 and Ist1 were added to the mix. This demonstrates the importance of Did2 and Ist1 for ESCRT-III-catalyzed membrane fission in the physiologically relevant orientation. Our data strongly support the notion that Vps4-catalyzed sequential conversion of Snf7-Vps2-Vps24 polymers to Did2-Ist1 polymers induces enough constriction of ESCRT-III assemblies to promote efficient membrane fission.

DISCUSSION

In this study, we report the discovery of a Vps4-driven polymerization sequence of ESCRT-III subunits that promotes membrane deformation and fission (Figures 7D and S7). Our analysis reveals three essential features of the ESCRT-III-mediated membrane fission reaction. First, we show that membrane deformation is coupled to changes of filament shape associated with changes of subunits stoichiometry. Second, we identify the last complex in the sequence, Did2-Ist1, as competent to promote membrane fission, and third, we show that the sequence orients the polymerization of ESCRT-III within membrane necks. Because the number and the redundancy of ESCRT-III subunits are highly variable between species, the molecular sequence we identified with yeast proteins may be different in other species. However, we expect these three central principles to be common to all.

In clathrin-mediated endocytosis, the sequence of subunit recruitment (Kaksonen et al., 2005; Taylor et al., 2011) is also coupled to membrane deformation. However, while semi-reconstituted assays established its dependence on ATP (Wu et al., 2010), this sequence has never been reconstituted *in vitro*. Thus, the ESCRT-III sequence we identified here is the first example of the *in vitro* reconstitution of a membrane remodeling process driven by sequential protein recruitment. Such a pathway had been postulated before from biochemical studies (Henne et al., 2012; Saksena et al., 2009; Teis et al., 2008), but it was never directly observed. Our study defines three essential parameters to control the temporal order of the sequence: the subunit affinity for the membrane, the specific affinity between subunits, as the preceding subunits recruit the subsequent, and the role of Vps4 which, by fueling the subunit turnover, drives unidirectional progression. These principal aspects of the ESCRT-III polymerization sequence are different from the clathrin endocytic sequence, where membrane curvature and phosphoinositide metabolism are crucial (Kaksonen and Roux, 2018). In our study, although membrane curvature may influence the dynamics of the sequence, we reconstituted the sequence onto non-deformable supported bilayers showing that curvature is not critical for driving the sequence.

We previously proposed, based on theoretical work (Lenz et al., 2009), that the flat Snf7-spirals buckle to induce curvature

Snf7+Vps2+Vps24+Vps4/ATP: n = 4, ROI = 110; Snf7 +Vps2+Vps24+Ist1+Vps4/ATP: n = 3, ROI = 105; Snf7+Vps2+Vps24+Did2+Vps4/ATP: n = 3, ROI = 48; Snf7+Vps2+Vps24+Did2+Ist1+Vps4: n = 3, ROI = 73; Snf7+Vps2+Vps24+ Did2+Ist1+Vps4/ATP: n = 6, ROI = 133; mean ± SD.
(D) Model of the coupling between ESCRT-III recruitment sequence and membrane remodeling activities (see also Figure S7).
See also Figure S5.

(Chiaruttini et al., 2015). While Snf7 filaments have all properties (growth and elasticity) to buckle, we never observed tubular protrusions with Snf7 filaments. Here, using both molecular dynamics simulations and experimental data, we find that the buckling transition is likely induced by the recruitment of ESCRT-III subunits that change the filament architecture. First addition of Vps2-Vps24, forms a secondary filament along Snf7 filaments (Mierzwa et al., 2017) and thereby rigidifies the polymer increasing its potential to buckle spontaneously (Henne et al., 2012; Moser von Filseck et al., 2020). Subsequently, the exchange of Vps24 to Did2 results in the formation of conical spirals. Finally, Vps4-mediated filament-removal triggers the formation of helical filaments. At the molecular level, we show that sequential assembly and disassembly of copolymers consisting of a flat (Snf7) and a helical (Vps2-Did2) filament mediate this buckling transition. Our simulations demonstrate that this depends on the two filaments having a different tilt in their membrane binding interface, relative to the main axis of the filament.

The final Did2-Ist1-assembly in the sequence, which was shown to constrict membrane tubes to 4.8 nm from their outside (Nguyen et al., 2020), is the only ESCRT-III polymer identified so far that is compatible with constriction sizes that lead to fission. However, the exact dimensions of the pre-fission intermediate constituted of Did2-Ist1 are not known, and its structure may differ from the equilibrium state presented in Nguyen et al. (2020). Furthermore, we find that Vps4 activity is required for constriction and fission. Thus, the ATPase might play a role in fission beyond establishment of the Did2-Ist1 polymer. Similar to dynamin-mediated membrane fission (Roux et al., 2006), additional external forces might be required to finalize the progression from highly constricted membrane structures toward fission. Possible origins of such forces during ESCRT-III activity could be protein- and cargo-crowding in ILV formation or cell migration in abscission. Did2-Ist1 can assemble around or inside membrane necks *in vivo* (Allison et al., 2013) and *in vitro* (McCullough et al., 2015) and induce fission in both orientations (our study). Understanding how the same complex, in different orientation, still constricts the membrane sufficiently to trigger fission, and whether other important players, such as cargoes (Mageswaran et al., 2015), are essential for fission, remains an open question for future studies.

To conclude, in this study, we find the principles of ESCRT-III activity to be an ATP-driven sequential subunit assembly and disassembly (polymerization sequence) that induces changes in ESCRT-III-polymer properties to trigger two steps of shape transitions: first, filament buckling (promoting membrane deformation) and then filament constriction (promoting membrane fission). The same principles have been suggested to apply to ESCRT-mediated abscission during archaea cytokinesis (Risa et al., 2019). Here, a ring formed of CdvB (archaeal ESCRT-III homolog) recruits two other homologs CdvB1 and CdvB2. Removal of CdvB then allows the constriction of the remaining CdvB1/2 ring that promotes membrane fission. These sequential changes in ESCRT-III filament structure that accompany membrane scission appear remarkably similar to the filament constriction pathway we observe here (Figure 6). Together with our mammalian cell data, these two *in vivo* examples highlight

how conserved the common principles of ESCRT-III activity discovered in this study are. While the subunit composition of the ESCRT-III filaments may vary from species to species, and from one cellular function to another, the common principles of a sequence of subunit exchanges, that shifts the architecture and mechanical properties of ESCRT-III filaments, knock together a general mechanism by which ESCRT-III remodels membranes.

STAR★METHODS

Detailed methods are provided in the online version of this paper and include the following:

- KEY RESOURCES TABLE
- RESOURCE AVAILABILITY
  ○ Lead Contact
  ○ Materials Availability
  ○ Data Availability
- EXPERIMENTAL MODEL AND SUBJECT DETAILS
  ○ Cell lines
- METHOD DETAILS
  ○ Protein purification
  ○ Preparation of giant unilamellar vesicles (GUV) and large giant unilamellar vesicles (LUV)
  ○ Supported membrane bilayer assay
  ○ Artificial membrane necks assay
  ○ Silication of Amine-polystyrene beads
  ○ Image acquisition
  ○ Electron microscopy
  ○ Optical tweezer tube pulling experiment
  ○ *In vitro* reconstitution of ESCRT-III sequence
  ○ Biochemical membrane fission assay
  ○ Membrane neck fission assay
  ○ Kinetics of CHMP4B and IST1 endosomal relocalization after hypertonic shock
  ○ Formation of protein polymers on bicelles
  ○ Molecular dynamics simulation
- QUANTIFICATION AND STATISTICAL ANALYSIS
  ○ SBL-bilayer assay and membrane necks
  ○ Cryo electron microscopy
  ○ Confocal imaging of mammalian cells
  ○ Molecular dynamics simulation

AUTHOR CONTRIBUTIONS

A.R. and A.-K.P. conceptualized the study. A.-K.P. performed and analyzed *in vitro*, negative stain EM, and cryo-freeze fracture EM experiments. V.M. performed and analyzed live-cell experiments. J.M.v.F. performed and analyzed cryo-EM experiments. A.R. supervised the project. The physical model was built by X.J., with guidance from A.Š. and B.B. A.-K.P. and A.R. wrote the manuscript with input of the other authors.

DECLARATION OF INTERESTS

The authors declare no competing interests.

REFERENCES

Adell, M.A.Y., Vogel, G.F., Pakdel, M., Müller, M., Lindner, H., Hess, M.W., and Teis, D. (2014). Coordinated binding of Vps4 to ESCRT-III drives membrane neck constriction during MVB vesicle formation. J. Cell Biol. *205*, 33–49.

Adell, M.A.Y., Migliano, S.M., Upadhyayula, S., Bykov, Y.S., Sprenger, S., Pakdel, M., Vogel, G.F., Jih, G., Skillern, W., Behrouzi, R., et al. (2017). Recruitment dynamics of ESCRT-III and Vps4 to endosomes and implications for reverse membrane budding. eLife *6*, e31652.

Agromayor, M., Carlton, J.G., Phelan, J.P., Matthews, D.R., Carlin, L.M., Ameer-Beg, S., Bowers, K., and Martin-Serrano, J. (2009). Essential role of hIST1 in cytokinesis. Mol. Biol. Cell *20*, 1374–1387.

Aguet, F., Van De Ville, D., and Unser, M. (2008). Model-based 2.5-d deconvolution for extended depth of field in brightfield microscopy. IEEE Trans. Image Process. *17*, 1144–1153.

Allison, R., Lumb, J.H., Fassier, C., Connell, J.W., Ten Martin, D., Seaman, M.N.J., Hazan, J., and Reid, E. (2013). An ESCRT-spastin interaction promotes fission of recycling tubules from the endosome. J. Cell Biol. *202*, 527–543.

Babst, M., Katzmann, D.J., Estepa-Sabal, E.J., Meerloo, T., and Emr, S.D. (2002). Escrt-III: an endosome-associated heterooligomeric protein complex required for mvb sorting. Dev. Cell *3*, 271–282.

Bajorek, M., Morita, E., Skalicky, J.J., Morham, S.G., Babst, M., and Sundquist, W.I. (2009a). Biochemical analyses of human IST1 and its function in cytokinesis. Mol. Biol. Cell *20*, 1360–1373.

Bajorek, M., Schubert, H.L., McCullough, J., Langelier, C., Eckert, D.M., Stublefield, W.-M.B., Uter, N.T., Myszka, D.G., Hill, C.P., and Sundquist, W.I. (2009b). Structural basis for ESCRT-III protein autoinhibition. Nat. Struct. Mol. Biol. *16*, 754–762.

Banjade, S., Tang, S., Shah, Y.H., and Emr, S.D. (2019). Electrostatic lateral interactions drive ESCRT-III heteropolymer assembly. eLife *8*, e46207.

Baum, D.A., and Baum, B. (2014). An inside-out origin for the eukaryotic cell. BMC Biol. *12*, 76.

Bleck, M., Itano, M.S., Johnson, D.S., Thomas, V.K., North, A.J., Bieniasz, P.D., and Simon, S.M. (2014). Temporal and spatial organization of ESCRT protein recruitment during HIV-1 budding. Proc. Natl. Acad. Sci. USA *111*, 12211–12216.

Boucrot, E., Pick, A., Çamdere, G., Liska, N., Evergren, E., McMahon, H.T., and Kozlov, M.M. (2012). Membrane fission is promoted by insertion of amphipathic helices and is restricted by crescent BAR domains. Cell *149*, 124–136.

Brune, T., Kunze-Schumacher, H., and Kölling, R. (2019). Interactions in the ESCRT-III network of the yeast Saccharomyces cerevisiae. Curr. Genet. *65*, 607–619.

Chiaruttini, N., and Roux, A. (2017). Dynamic and elastic shape transitions in curved ESCRT-III filaments. Curr. Opin. Cell Biol. *47*, 126–135.

Chiaruttini, N., Redondo-Morata, L., Colom, A., Humbert, F., Lenz, M., Scheuring, S., and Roux, A. (2015). Relaxation of Loaded ESCRT-III Spiral Springs Drives Membrane Deformation. Cell *163*, 866–879.

Christ, L., Wenzel, E.M., Liestøl, K., Raiborg, C., Campsteijn, C., and Stenmark, H. (2016). ALIX and ESCRT-I/II function as parallel ESCRT-III recruiters in cytokinetic abscission. J. Cell Biol. *212*, 499–513.

Danino, D., Moon, K.-H., and Hinshaw, J.E. (2004). Rapid constriction of lipid bilayers by the mechanochemical enzyme dynamin. J. Struct. Biol. *147*, 259–267.

Dasgupta, R., and Dimova, R. (2014). Inward and outward membrane tubes pulled from giant vesicles. J. Phys. D Appl. Phys. *47*, 282001.

Effantin, G., Dordor, A., Sandrin, V., Martinelli, N., Sundquist, W.I., Schoehn, G., and Weissenhorn, W. (2013). ESCRT-III CHMP2A and CHMP3 form variable helical polymers in vitro and act synergistically during HIV-1 budding. Cell. Microbiol. *15*, 213–226.

Fyfe, I., Schuh, A.L., Edwardson, J.M., and Audhya, A. (2011). Association of the endosomal sorting complex ESCRT-II with the Vps20 subunit of ESCRT-III generates a curvature-sensitive complex capable of nucleating ESCRT-III filaments. J. Biol. Chem. *286*, 34262–34270.

Ghaemmaghami, S., Huh, W.-K., Bower, K., Howson, R.W., Belle, A., Dephoure, N., O'Shea, E.K., and Weissman, J.S. (2003). Global analysis of protein expression in yeast. Nature *425*, 737–741.

Guizetti, J., Schermelleh, L., Mäntler, J., Maar, S., Poser, I., Leonhardt, H., Müller-Reichert, T., and Gerlich, D.W. (2011). Cortical constriction during abscission involves helices of ESCRT-III-dependent filaments. Science *331*, 1616–1620.

Hanson, P.I., Roth, R., Lin, Y., and Heuser, J.E. (2008). Plasma membrane deformation by circular arrays of ESCRT-III protein filaments. J. Cell Biol. *180*, 389–402.

Harker-Kirschneck, L., Baum, B., and Šarić, A.E. (2019). Changes in ESCRT-III filament geometry drive membrane remodelling and fission in silico. BMC Biol. *17*, 82.

Heinzle, C., Mücke, L., Brune, T., and Kölling, R. (2019). Comprehensive analysis of yeast ESCRT-III composition in single ESCRT-III deletion mutants. Biochem. J. *476*, 2031–2046.

Henne, W.M., Buchkovich, N.J., Zhao, Y., and Emr, S.D. (2012). The endosomal sorting complex ESCRT-II mediates the assembly and architecture of ESCRT-III helices. Cell *151*, 356–371.

Hierro, A., Sun, J., Rusnak, A.S., Kim, J., Prag, G., Emr, S.D., and Hurley, J.H. (2004). Structure of the ESCRT-II endosomal trafficking complex. Nature *431*, 221–225.

Johnson, D.S., Bleck, M., and Simon, S.M. (2018). Timing of ESCRT-III protein recruitment and membrane scission during HIV-1 assembly. eLife *7*, e36221.

Kaksonen, M., and Roux, A. (2018). Mechanisms of clathrin-mediated endocytosis. Nat. Rev. Mol. Cell Biol. *19*, 313–326.

Kaksonen, M., Toret, C.P., and Drubin, D.G. (2005). A modular design for the clathrin- and actin-mediated endocytosis machinery. Cell *123*, 305–320.

Kozlovsky, Y., and Kozlov, M.M. (2002). Stalk model of membrane fusion: solution of energy crisis. Biophys. J. *82*, 882–895.

Lata, S., Schoehn, G., Jain, A., Pires, R., Piehler, J., Gottlinger, H.G., and Weissenhorn, W. (2008). Helical structures of ESCRT-III are disassembled by VPS4. Science *321*, 1354–1357.

Lee, I.-H., Kai, H., Carlson, L.-A., Groves, J.T., and Hurley, J.H. (2015). Negative membrane curvature catalyzes nucleation of endosomal sorting complex required for transport (ESCRT)-III assembly. Proc. Natl. Acad. Sci. USA *112*, 15892–15897.

Lenz, M., Crow, D.J.G., and Joanny, J.-F. (2009). Membrane buckling induced by curved filaments. Phys. Rev. Lett. *103*, 038101.

Mageswaran, S.K., Johnson, N.K., Odorizzi, G., and Babst, M. (2015). Constitutively active ESCRT-II suppresses the MVB-sorting phenotype of ESCRT-0 and ESCRT-I mutants. Mol. Biol. Cell *26*, 554–568.

Maity, S., Caillat, C., Miguet, N., Sulbaran, G., Effantin, G., Schoehn, G., Roos, W.H., and Weissenhorn, W. (2019). VPS4 triggers constriction and cleavage of ESCRT-III helical filaments. Sci. Adv. 5, eaau7198.

McCullough, J., Clippinger, A.K., Talledge, N., Skowyra, M.L., Saunders, M.G., Naismith, T.V., Colf, L.A., Afonine, P., Arthur, C., Sundquist, W.I., et al. (2015). Structure and membrane remodeling activity of ESCRT-III helical polymers. Science 350, 1548–1551.

Mercier, V., Larios, J., Molinard, G., Goujon, A., Matile, S., Gruenberg, J., and Roux, A. (2019). Endosomal Membrane Tension Regulates ESCRT-III-Dependent Intra-Lumenal Vesicle Formation. bioRxiv. https://doi.org/10.1101/550483.

Mierzwa, B.E., Chiaruttini, N., Redondo-Morata, L., von Filseck, J.M., König, J., Larios, J., Poser, I., Müller-Reichert, T., Scheuring, S., Roux, A., and Gerlich, D.W. (2017). Dynamic subunit turnover in ESCRT-III assemblies is regulated by Vps4 to mediate membrane remodelling during cytokinesis. Nat. Cell Biol. 19, 787–798.

Morlot, S., Galli, V., Klein, M., Chiaruttini, N., Manzi, J., Humbert, F., Dinis, L., Lenz, M., Cappello, G., and Roux, A. (2012). Membrane shape at the edge of the dynamin helix sets location and duration of the fission reaction. Cell 151, 619–629.

Moser von Filseck, J., Barberi, L., Talledge, N., Johnson, I.E., Frost, A., Lenz, M., and Roux, A. (2020). Anisotropic ESCRT-III architecture governs helical membrane tube formation. Nat. Commun. 11, 1516.

Nguyen, H.C., Talledge, N., McCullough, J., Sharma, A., Moss, F.R., 3rd, Iwasa, J.H., Vershinin, M.D., Sundquist, W.I., and Frost, A. (2020). Membrane constriction and thinning by sequential ESCRT-III polymerization. Nat. Struct. Mol. Biol. 27, 392–399.

Nickerson, D.P., West, M., and Odorizzi, G. (2006). Did2 coordinates Vps4-mediated dissociation of ESCRT-III from endosomes. J. Cell Biol. 175, 715–720.

Obita, T., Saksena, S., Ghazi-Tabatabai, S., Gill, D.J., Perisic, O., Emr, S.D., and Williams, R.L. (2007). Structural basis for selective recognition of ESCRT-III by the AAA ATPase Vps4. Nature 449, 735–739.

Plimpton, S. (1995). Fast Parallel Algorithms for Short-Range Molecular Dynamics. J. Comp. Phys. 117, 1–19.

Poser, I., Sarov, M., Hutchins, J.R.A., Hériché, J.-K., Toyoda, Y., Pozniakovsky, A., Weigl, D., Nitzsche, A., Hegemann, B., Bird, A.W., et al. (2008). BAC TransgeneOmics: a high-throughput method for exploration of protein function in mammals. Nat. Methods 5, 409–415.

Risa, G.T., Hurtig, F., Bray, S., Hafner, A.E., Harker-Kirschneck, L., Faull, P., Davis, C., Papatziamou, D., Mutavchiev, D.R., Fan, C., et al. (2019). Proteasome-mediated protein degradation resets the cell division cycle and triggers ESCRT-III-mediated cytokinesis in an archaeon. bioRxiv. https://doi.org/10.1101/774273.

Roux, A., Uyhazi, K., Frost, A., and De Camilli, P. (2006). GTP-dependent twisting of dynamin implicates constriction and tension in membrane fission. Nature 441, 528–531.

Saksena, S., Wahlman, J., Teis, D., Johnson, A.E., and Emr, S.D. (2009). Functional reconstitution of ESCRT-III assembly and disassembly. Cell 136, 97–109.

Schindelin, J., Arganda-Carreras, I., Frise, E., Kaynig, V., Longair, M., Pietzsch, T., Preibisch, S., Rueden, C., Saalfeld, S., Schmid, B., et al. (2012). Fiji: an open-source platform for biological-image analysis. Nat. Methods 9, 676–682.

Schöneberg, J., Lee, I.-H., Iwasa, J.H., and Hurley, J.H. (2017). Reverse-topology membrane scission by the ESCRT proteins. Nat. Rev. Mol. Cell Biol. 18, 5–17.

Schöneberg, J., Pavlin, M.R., Yan, S., Righini, M., Lee, I.-H., Carlson, L.-A., Bahrami, A.H., Goldman, D.H., Ren, X., Hummer, G., et al. (2018). ATP-dependent force generation and membrane scission by ESCRT-III and Vps4. Science 362, 1423–1428.

Shen, Q.-T., Schuh, A.L., Zheng, Y., Quinney, K., Wang, L., Hanna, M., Mitchell, J.C., Otegui, M.S., Ahlquist, P., Cui, Q., and Audhya, A. (2014). Structural analysis and modeling reveals new mechanisms governing ESCRT-III spiral filament assembly. J. Cell Biol. 206, 763–777.

Simunovic, M., Manneville, J.-B., Renard, H.-F., Evergren, E., Raghunathan, K., Bhatia, D., Kenworthy, A.K., Voth, G.A., Prost, J., McMahon, H.T., et al. (2017). Friction Mediates Scission of Tubular Membranes Scaffolded by BAR Proteins. Cell 170, 172–184.

Stuchell-Brereton, M.D., Skalicky, J.J., Kieffer, C., Karren, M.A., Ghaffarian, S., and Sundquist, W.I. (2007). ESCRT-III recognition by VPS4 ATPases. Nature 449, 740–744.

Szwedziak, P., Wang, Q., Bharat, T.A.M., Tsim, M., and Löwe, J. (2014). Architecture of the ring formed by the tubulin homologue FtsZ in bacterial cell division. eLife 3, e04601.

Talledge, N., McCullough, J., Wenzel, D., Nguyen, H.C., Lalonde, M.S., Bajorek, M., Skalicky, J., Frost, A., and Sundquist, W.I. (2018). The ESCRT-III proteins IST1 and CHMP1B assemble around nucleic acids. bioRxiv. https://doi.org/10.1101/386532.

Tan, J., Davies, B.A., Payne, J.A., Benson, L.M., and Katzmann, D.J. (2015). Conformational Changes in the Endosomal Sorting Complex Required for the Transport III Subunit Ist1 Lead to Distinct Modes of ATPase Vps4 Regulation. J. Biol. Chem. 290, 30053–30065.

Taylor, M.J., Perrais, D., and Merrifield, C.J. (2011). A high precision survey of the molecular dynamics of mammalian clathrin-mediated endocytosis. PLoS Biol. 9, e1000604.

Teis, D., Saksena, S., and Emr, S.D. (2008). Ordered assembly of the ESCRT-III complex on endosomes is required to sequester cargo during MVB formation. Dev. Cell 15, 578–589.

Teis, D., Saksena, S., Judson, B.L., and Emr, S.D. (2010). ESCRT-II coordinates the assembly of ESCRT-III filaments for cargo sorting and multivesicular body vesicle formation. EMBO J. 29, 871–883.

Vietri, M., Radulovic, M., and Stenmark, H. (2020). The many functions of ESCRTs. Nat. Rev. Mol. Cell Biol. 21, 25–42.

Vietri, M., Schink, K., Campsteijn, C., Wegner, C., Schultz, S., Christ, L., Thoresen, S., Brech, A., Raiborg, C., and Stenmark, H. (2015). Spastin and ESCRT-III coordinate mitotic spindle disassembly and nuclear envelope sealing. Nature 522, 231–235.

Wollert, T., Wunder, C., Lippincott-Schwartz, J., and Hurley, J.H. (2009). Membrane scission by the ESCRT-III complex. Nature 458, 172–177.

Wu, M., Huang, B., Graham, M., Raimondi, A., Heuser, J.E., Zhuang, X., and De Camilli, P. (2010). Coupling between clathrin-dependent endocytic budding and F-BAR-dependent tubulation in a cell-free system. Nat. Cell Biol. 12, 902–908.

Xiao, J., Chen, X.-W., Davies, B.A., Saltiel, A.R., Katzmann, D.J., and Xu, Z. (2009). Structural basis of Ist1 function and Ist1-Did2 interaction in the multivesicular body pathway and cytokinesis. Mol. Biol. Cell 20, 3514–3524.

Yang, B., Stjepanovic, G., Shen, Q., Martin, A., and Hurley, J.H. (2015). Vps4 disassembles an ESCRT-III filament by global unfolding and processive translocation. Nat. Struct. Mol. Biol. 22, 492–498.

Yuan, H., Huang, C., Li, J., Lykotrafitis, G., and Zhang, S. (2010). One-particle-thick, solvent-free, coarse-grained model for biological and biomimetic fluid membranes. Phys. Rev. E Stat. Nonlin. Soft Matter Phys. 82, 011905.

STAR★METHODS

KEY RESOURCES TABLE

REAGENT or RESOURCE	SOURCE	IDENTIFIER
Bacterial and Virus Strains		
Rosetta2	Novagen	Cat#: 71397
Chemicals, Peptides, and Recombinant Proteins		
IPTG	Sigma -Aldrich	CAS: https://www.sigmaaldrich.com/catalog/search?term=7647-14-5&interface=CAS No.&N=0&mode=partialmax&lang=en&region=US&focus=product; 10724815001
HEPES	Applichem	CAS: 7365-45-9; A3724
NaCl	Sigma-Aldrich	CAS: https://www.sigmaaldrich.com/catalog/search?term=367-93-1&interface=CAS No.&N=0&mode=partialmax&lang=en&region=US&focus=product; 1162241000
Triton X-100	Applichem	CAS: 9002-93-1; A4975
cOmplete	Roche	Cat#: 11873580001
HisTrap	GE Healthcare	GE29-0510-21
Imidazole	Applichem	CAS: 9002-93-1288-32-4; A1378
Superdex 200 26/60	GE Healthcare	GE28-9893-36
b-Mercaptoethanol	Applichem	CAS: 60-24-2; A1108
Tris	Applichem	CAS: 77-86-1; A1379
DTT	Applichem	CAS: https://www.sigmaaldrich.com/catalog/search?term=3483-12-3&interface=CAS No.&N=0+&mode=partialmax&lang=en&region=US&focus=product; https://www.sigmaaldrich.com/catalog/product/sigma/d9779?lang=en&region=US
TFP-AlexaFluor-488	ThermoFisher Scientific	Cat#: A37570
TFP-Atto-565	Atto-Tec	AD 565-3
maleimide-Atto-565	Atto-Tec	AD 565-4
maleimide-AlexFluor-488	ThermoFisher Scientific	Cat#: A10254
DOPC	Avanti Polar Lipids	Cat#: https://www.sigmaaldrich.com/catalog/product/avanti/850375C
DOPS	Avanti Polar Lipids	Cat#: https://www.sigmaaldrich.com/catalog/product/avanti/840035C
DOPE-Atto647N	Atto-tec	Cat#: AD 647N-16
DSPE-PEG(2000)Biotin	Avanti Polar Lipids	Cat#: https://www.sigmaaldrich.com/catalog/product/avanti/880129P
Rhodamine-PE	Avanti Polar Lipids	Cat#: https://www.sigmaaldrich.com/catalog/product/avanti/810150P
$MgCl_2$	Acros Organics	CAS: 7786-30-3; 223210025
Casein	Sigma -Aldrich	CAS: https://www.sigmaaldrich.com/catalog/search?term=9000-71-9&interface=CAS No.&N=0+&mode=partialmax&lang=en&region=US&focus=product ; https://www.sigmaaldrich.com/catalog/product/sigma/c6905?lang=en&region=US
Avidin	Sigma -Aldrich	CAS: https://www.sigmaaldrich.com/catalog/search?term=1405-69-2&interface=CAS No.&N=0+&mode=partialmax&lang=en&region=US&focus=product ; https://www.sigmaaldrich.com/catalog/product/sigma/a9275?lang=en&region=US

(Continued on next page)

Continued

REAGENT or RESOURCE	SOURCE	IDENTIFIER
biotinylated-Albumin	Sigma-Aldrich	CAS: https://www.sigmaaldrich.com/catalog/search?term=9048-46-8&interface=CAS No.&N=0+&mode=partialmax&lang=en&region=US&focus=product ;
silica beads 1μm	Bangs Laboratories	Cat#: SS04000
silica beads 2μm	Bangs Laboratories	Cat#: SS04002
NH$_2$-PS beads 27 nm	Bangs Laboratories	Cat#: PS02001
Sucrose	Applichem	CAS: 57-50-1; A2211
Glycerol	Applichem	CAS: 56-81-5; A1123
TEOS	Sigma-Aldrich	CAS: https://www.sigmaaldrich.com/catalog/search?term=78-10-4&interface=CAS No.&N=0&mode=partialmax&lang=en&region=US&focus=product; 759414
isopropanol	Acros Organics	CAS: 67-63-0; 149320025
uranyl acetate	Polysciences	Cat#: 21447-25
ATP	Roche	CAS: https://www.sigmaaldrich.com/catalog/search?term=51963-61-2&interface=CAS No.&N=0&mode=partialmax&lang=en&region=US&focus=product; 10519979001
DMEM	Thermo Fisher Scientific	Cat#: 10566016
Leibovitz's	Thermo Fisher Scientific	Cat#: 11415064
BD Difco LB Broth Lennox	Thermo Fisher Scientific	Cat#: 11798842
CHAPS (3-[(3-Cholamidopropyl)-dimethyl-ammonio]-1-propanesulfonate hydrate	Sigma-Aldrich	CAS: https://www.sigmaaldrich.com/catalog/search?term=331717-45-4&interface=CAS No.&N=0&mode=partialmax&lang=en&region=US&focus=product; 226947
Deposited Data		
Raw and analyzed data	This paper	https://zenodo.org/record/3878199
Experimental Models: Cell Lines		
HeLa Kyoto GFP-CHMP4B	Poser et al., 2008	N/A
HeLa Kyoto IST1-mCherry	Vietri et al., 2015	N/A
Recombinant DNA		
pST39-Vps25(1-203) - His/Vps22(1-234) - Vps36 (1-567) (ESCRT-II)	Hierro et al., 2004	Addgene #17633
pMBP-HIS2-Vps20FL	Wollert et al., 2009	Addgene #21490
pMBP-HIS2-Snf7	Wollert et al., 2009	Addgene #21492
pMBP-HIS2-Vps2	Wollert et al., 2009	Addgene #21494
https://wayf.switch.ch/SWITCHaai/WAYF?entityID=https%3A%2F%2Fwww.unige.ch%2Fshibboleth&return=https%3A%2F%2Fwww.unige.ch%2FShibboleth.sso%2FLogin%3FSAMLDS%3D1%26target%3Dss%253Amem%253A21e3bae973f73f97b6f6d894296f90f5131594f8bfef33ea170b2278ab26f73c	Wollert et al., 2009	N/A
pGST-Vps4	Wollert et al., 2009	Addgene #21495
pET28b Did2-His6	Tan et al., 2015	N/A
pET28b His6-Ist1	Tan et al., 2015	N/A
Software and Algorithms		
Lammps code	Plimpton, 1995	https://lammps.sandia.gov
Fiji	Schindelin et al., 2012	https://imagej.net/Fiji

RESOURCE AVAILABILITY

Lead Contact
Further information and requests for resources and reagents should be directed to and will be fulfilled by the Lead Contact, Aurélien Roux (Aurelien.Roux@unige.ch).

Materials Availability
This study did not generate new unique reagents.

Data Availability
The original uncropped images stacks from which the kymographs shown in main and supplementary figures were extracted and fluorescence intensities values used in quantifications are available through: https://zenodo.org/record/3878199.

EXPERIMENTAL MODEL AND SUBJECT DETAILS

Cell lines
We obtained HeLa Kyoto cells stably expressing GFP-CHMP4B from Anthony Hyman (MPI-CBG, Dresden) (Poser et al., 2008). They were authenticated by Microsynth (Balgach, Switzerland), which revealed 100% identity to the DNA profile of the cell line HeLa (ATCC: CCL-2) and 100% identity over all 15 autosomal STRs to the Microsynth's reference DNA profile of HeLa. We obtained HeLa Kyoto cells stably expressing Ist1-mCherry from Harald Stenmark (Vietri et al., 2015). HeLa Kyoto cells are female. HeLa Kyoto cells were cultured in DMEM supplemented with 10% FBS and 2% penicillin-streptomycin at 37°C and 5% CO_2.

We used Rosetta2 *E. coli* for protein production. Bacteria were cultured in LB-medium at 37°C.

METHOD DETAILS

Protein purification
ESCRT-II (Addgene plasmid #17633), Vps20 (Addgene plasmid #21490), Snf7(Addgene plasmid #21492), Vps2 (Addgene plasmid #21494), Vps24 (kind gift from James Hurley lab, UC Berkeley, USA) and Vps4 (Addgene plasmid #21495) were expressed and purified as previously described (Hierro et al., 2004; Wollert et al., 2009). In detail, proteins were expressed at 20°C overnight in Rosetta2 (induction 0.5M IPTG), before lysis by sonication (lysis buffer: 20 mM HEPES pH7.4, 100 mM NaCl, 1% Triton, cOmplete) and HisTrap purification (elution buffer: 20 mM HEPES pH7.4, 100mM NaCl, 100 mM Imidazole). MBP-His-tag was cleaved off using TEV followed by purification on a Superdex 200 26/60 column (buffer: 20mM HEPES pH 8.0).

Did2 and Ist1 (gift from David Katzmann lab, Mayo clinic, USA) were expressed and purified as previously described (Tan et al., 2015). In detail, proteins were expressed at 30°C overnight in Rosetta2 (induction 0.5M IPTG), before lysis by sonication (lysis buffer: 50mM Tris pH8.5, 5mM β-Mercaptoethanol, 1% Triton, cOmplete). The proteins were purified using a HisTrap (elution buffer: 50mM Tris pH8.5, 5mM β-Mercaptoethanol, 1M Imidazole) followed by dialyses (buffer: 50mM Tris pH 7.5, 150mM NaCl, 2mM DTT) to remove the Imidazole.

Following the labeling procedure given by the reagent provider, Snf7, Vps2, Ist1 and Vps24 were labeled with TFP-AlexaFluor-488 (Ref N°A-30005, ThermoFisher Scientific,). Vps2 and Vp24 were labeled with TFP-Atto-565 (Atto-Tec AD 565-3). Did2 and Ist1 were labeled with maleimide-Atto-565 (Atto-Tec AD 565-3). Did2 was labeled with maleimide-AlexFluor-488 (ThermoFisher Scientific, A-30005). If not otherwise mentioned, following protein concentration were used: ESCRT-II 1μM, Vps20 1μM, Snf7 500nM, Did2 1 μM, Ist1 1 μM, Vps4 1 μM, ATP 2 mM. In Figure S6E 100nM Vps2 and Vps24 were used. In experiments including Did2 Vps2 and Vps24 concentration were scaled up to 1 μM to match Did2 concentration. In general, labeled proteins were mixed 1:1 with unlabeled protein.

Preparation of giant unilamellar vesicles (GUV) and large giant unilamellar vesicles (LUV)
GUVs were prepared by electroformation: 20-30 μL of a 2mg/ml lipid solution in chloroform (DOPC:DOPS:DOPE-Atto647N:DSPE-PEG(2000)Biotin, 6:4:0.01:0.003; Avanti Polar Lipids, Atto-tec) were dried on indium-tin oxide (ITO)-coated glass slides for 1h. A growth chamber was assembled by clamping a rubber ring between the ITO-slides, filled with 500 μL of a sucrose buffer osmotically equilibrated with the experimental buffer. ITO-Slides were then connected to an AC generator set under 1V AC (10 Hz) for 1.5h. GUVs were stored at 4°C for at maximum a week.

For LUV preparation, DOPC:DOPS:Rhodamine-PE (6:4:1; 10 mg/ml) mixture was evaporated in a glass tube, 500 μL of buffer were added, the tube was vortex followed by 5 times freezing and thawing. LUVs were stored at −20°C until usage.

Supported membrane bilayer assay
Supported membrane bilayer assay was performed as described in Chiaruttini et al. (2015). Experiments were performed in 20 mM Tris pH.6.8, 200 mM NaCl and 1 mM MgCl₂. 2 mM DTT was added to the buffer for experiments including Ist1. GUVs diluted in buffer

were burst on a plasma-cleaned coverslip forming the bottom of a flow chamber (coverslip and sticky-Slide VI 0.4, Ibidi) to form supported bilayers. Thereafter, the chamber was passivated with Casein (1mg/ml Sigma-Aldrich) for 10 min and washed with buffer, before the experiments was conducted. Subsequent changes of protein or buffer solutions in the chamber were made via a syringe pump connected to the flow chamber.

For comparison of the binding and disassembly kinetics of subunits (Figures 1C and 3A), two subunits out of the complete mix ((Snf7,) Vps2, Vps24, Did2, Ist1) were added as their labeled version (either Alexa488- or Atto565-) to unlabeled pre-grown Snf7-patches and their fluorescence was measured overtime. Then, the obtained single graphs were aligned using the time point of protein- or Vps4-addition, respectively.

Artificial membrane necks assay

For artificial membrane necks, partially adhered vesicles were prepared as described in Chiaruttini et al. (2015). Briefly, a flow chamber assembled from a coverslip and sticky-Slide VI 0.4, Ibidi was incubated with Avidin (0.1 mg/ml) for 10 min, before washing with buffer (20 mM Tris pH.6.8, 200 mM NaCl and 1mM $MgCl_2$) and addition of GUVs (including 0.03 % DSPE-PEG(2000)Biotin) diluted in buffer. As soon as GUVs started to attach biotinylated-Albumin (1mg/ml, Sigma-Aldrich) was added to stop attachment and prevent bursting of the GUVs. After 15 min of incubation, the chamber was washed with 3 chamber volumes of buffer and glass beads diluted in buffer were added (1μm beads, 1:500; 2μm beads, 1:200; Bangs Laboratories), which were nearly completely engulfed into attached GUV due to the adhesive forces between glass and lipids.

For artificial necks preparation for EM, LUVs, formed in 500 mOsm sucrose, were diluted 1:100 in buffer (20 mM Tris pH.6.8, 200 mM NaCl and 1mM $MgCl_2$), spun down (10', 5,000 g) and resuspended in buffer containing 27 nm silicated NH_2-PS beads (1:10). Mixture was then vortexed for 30 s and incubated for 1h at RT before loading on a 75% Sucrose cushion in a centrifuge tube, topped with buffer and centrifuged 20', 5,000 g to separate bead-containing vesicles from excessive beads. The floating layer containing the Rhodamine-labeled vesicles was carefully harvested, washed, and resuspended in buffer containing 30% glycerol and processed identical to freeze-fracture samples.

Silication of Amine-polystyrene beads

40.5 mL isopropanol and 8 mL ddH_2O were mixed and pH was adjusted to 11.3 using ammonia solution. 27 nm NH_2-PS beads (Bangs Laboratories) were sonicated (5 min), before 200 μL beads and 193 μL Tetraethylorthosilicat (TEOS) were added to the isopropanol/water mixture under stir. After incubation for 1h, beads were spun down 15' 13,000 g, washed twice with water and finally resuspended in 0.5 mL buffer. Beads were stored at 4°C until usage.

Image acquisition

Confocal Imaging was performed on an inverted spinning disc microscope assembled by 3i (Intelligent Imaging Innovation) consisting of a Nikon base (Eclipse C1, Nikon), a 100x 1.49 NA oil immersion objective and an EVOLVE EM-CCD camera (Ropper Scientific Inc.). For analysis of supported bilayer experiments, 3 μm thick Z stack were maximally projected using a Fiji plugin (Aguet et al., 2008). X-y drift of the microscopy was corrected using the plugin Turboreg and a custom-written ImageJ macro. For artificial membrane neck experiments, 15 μm thick Z stacks were acquired.

Electron microscopy

For EM experiments involving Snf7, LUVs were diluted 1:100 in buffer (20 mM Tris pH.6.8, 200 mM NaCl and 1mM $MgCl_2$), spun down (10', 5,000 g), resuspended in 4.5μM Snf7 for 6h (4°C), before 1 μM Vps2, 1 μM Vps24, 2 μM Did2 and 2 μM Ist1 were added overnight at 4°C.

In the experiments analyzing the number of strands per filament (Figures 1C and S1E), in comparison to data from Mierzwa et al. (2017), higher concentrations and longer incubation times of Vps2-Vps24 were used to ensure comparability with the experiments including Vps2-Did2, for which high concentration and long incubation were required due to its low affinity for Snf7. High concentration and long incubation of Vps2-Vps24 result in increased filament bundling a phenomena we (data not shown) and other using different ESCRT-III filaments (Banjade et al., 2019) observed previously. However, the clear prevalence of multimer-of-2 strands per filament strongly indicates the occurrence of the lateral co-polymerization we described in Mierzwa et al. (2017).

In experiments with Vps4, 1 μM Vps4, 2 mM ATP and 1 mM $MgCl_2$ were added to the samples the next morning, and incubated at 30°C for 30 min. To stop Vps4 activity, samples were chilled on ice and diluted 1:100 in buffer containing 50 mM EDTA. Finally, all samples were spun down 10' 5,000 g and resuspended in buffer (negative stain EM) or buffer containing 30% glycerol (cryofreeze-fracture). Negative stain samples were absorbed onto EM grids and stained with 2% uranyl acetate for 30 s. Freeze fracture samples were transferred onto sample stamps, flash-frozen and processed using a 060 Freeze-Fracture System (BAF). To grow Vps2-Did2(-Ist1) membrane tubes, 50 μl LUVs (10mg/ml) were diluted in buffer, spun 10' 5,000 g and incubated with 6 μM of Vps2, Did2 and Ist1 for 60h (4°C). Samples were treated with Vps4/ATP as follow: 1 μM Vps4, 2 mM ATP and 1 mM $MgCl_2$ were either added in solution for 30 min at 30°C to 1:5 diluted samples or to 1:20 diluted samples absorbed for 5 min onto an EM-grid.

Depolymerization in solution was stopped as described above. Depolymerization on grids was stopped by blotting and staining. Images were acquired on a Tecnai G2 Sphera (FEI) electron microscope.

Optical tweezer tube pulling experiment

Membrane nanotube pulling experiments were performed on the setup published in Chiaruttini et al. (2015) allowing simultaneous optical tweezer application, spinning disc confocal and brightfield imaging based on an inverted Nikon eclipse Ti microscope and a 5W 1064nm laser focused through a 100 × 1.3 NA oil objective (ML5-CW-P-TKS-OTS, Manlight). Outward directed membrane nanotubes were pulled with streptavidin beads (3.05 μm, Spherotec) from a GUV containing 0.01% DSPE-PEG(2000)Biotin and aspired in a motorized micropipette (MP-285, Sutter Instrument). Proteins were injected using a slightly bigger micropipette connected to a pressure control system (MFCS-VAC −69 mbar, Fluigent). 2 μm glass beads internalized into GUVs adhered on the bottom of flow chambers (see artificial membrane necks protocol) were pulled inward to form membrane nanotubes by moving the stage relative to the bead trapped in optical tweezers. Proteins were added via a syringe pump connected to the flow chamber. Radius r of outward pulled membrane nanotubes were calculated from the force F and membrane rigidity κ (κ = 12 kT) using the formula r = $(2\pi\kappa)$/F. F was determined following Hook's law F = k*Δx using the bead displacement and the trap stiffness k (k = 79 pN/nm/W). Radii of inward pulled tubes were estimated using mean fluorescence intensity of the tubes and a calibration curve (Figure S2A) which was established from outward pulled tubes. By changing the aspiration pressure in the pipette, the tension, and the radius of the tube can be changed.

In vitro reconstitution of ESCRT-III sequence

To reconstitute the ESCRT-III sequence, Snf7-patches were pre-grown on membrane bilayers and washed with 3 chamber volumes of buffer. Then, 2 μM Alexa488-Snf7, 1 μM Vps24, 800 nM Vps2, 1.5 μM Did2, 1 μM Ist1, 1.5 μM Vps4 and 10 mM ATP were added to the pre-grown patches. To ensure maximal activity of the ATPase throughout the reconstitution, we used a higher ATP (10 mM) concentration than typically found in cells (2 mM). We did not observe noticeable changes in the kinetics of any protein as compared to experiments done at 2 mM, besides a faster Did2 disassembly in conditions where it disassembled. Atto565-Vps2, Atto565-Vps24, Alexa488-Ist1 or Atto565-Did were mixed 1:1 with unlabeled protein. Vps2, Vps24, Ist1 and Did2 dynamics were imaged separately, but together with either Alexa488-Snf7 or Atto565-Vps2 to provide a time reference. To align the experiments on the time axis a scaling factor was calculated from the fluorescence intensity curve of Snf7 or Vps2. All experiments were rescaled with this factor proportional to the time of the peak, and the time at which it reached the lower plateau value after depolymerization and the distance between these time points (Figure S2A). Vps24, Vps2 and Did2 graphs were aligned using the calculated scaling factor from Snf7. Ist1 graph was aligned using the calculated scaling factor from Vps2 (Figure 4A).

Biochemical membrane fission assay

Membrane fission assay was adapted from Boucrot et al. (2012). Briefly, Vps2-Did2(-Ist1) membrane tubes were grown as described above. After incubation with Vps4 and ATP, liposomes were spun 15' at 250.000 g, 4°C, supernatant and pellet were mixed with sample buffer and separated using SDS-PAGE at 4°C. Gels were stained with 0.1% Coomassie in 10% acetic acid and destained in ddH$_2$O. Bands were quantified using ImageJ (Schindelin et al., 2012).

Membrane neck fission assay

Artificial membrane necks generated by 1 μm beads were incubated first with ESCRT-II, Vps20 and Snf7 for 5', followed by 15' incubation with Vps2, Vps24, Did2, Ist1, Vps4 and ATP, before the protein-mixture was replaced by buffer. Beads were pulled toward the center of the GUV with an optical trap and then released. Beads connected to the membrane of the GUV instantly retracted after release, in contrast to unconnected beads which stay in the center of the GUV.

Kinetics of CHMP4B and IST1 endosomal relocalization after hypertonic shock

For live-cell imaging, HeLa Kyoto cells stably expressing LAT-CHMP4B-GFP or LAT-IST1-mcherry were seeded at 1 to 1 ratio into 35mm MatTek glass bottom microwell dishes (MatTek Corporation). Before imaging, cells were rinsed 2-fold with 1ml Leibovitz's live imaging medium (Life Technologies, Thermofisher) so that cells could be incubated without CO2 equilibration at room temperature. Cells were imaged using a 100x 1.4 NA oil DIC Plan-Apochromat VC objective (Nikon) with a Nikon A1 scanning confocal microscope at speed of 1 frame every 2 minutes. Hypertonic shock was done by addition of 0.5M sucrose containing Leibovitz's medium for a final osmolarity of 900 mOsm.

Formation of protein polymers on bicelles

We prepared micelles by solubilizing a dried lipid film made from DOPC/DOPS (60/40 mol/mol) at 25°C in 100 mM NaCl, 20 mM HEPES pH = 7.5, 20 mM CHAPS (3-[(3-Cholamidopropyl)-dimethyl-ammonio]-1-propanesulfonate hydrate, Sigma-Aldrich) at a total lipid concentration of 12 mM. The following protocol is adapted from Szwedziak et al. (2014). In brief, micelles were homogenized by bath sonication and stirring at 25°C for 1 h before addition of 4 μM Snf7, 2 μM Vps24 and 2 μM Vps2, making sure that the detergent

concentration was above its critical micellar concentration after addition of all proteins. The sample was then gradually diluted four-fold over 30 min under agitation at 25°C and further incubated for 5 h. For cryo-EM, 4 μL of the sample were deposited on glow-discharged Quantifoil R1.2/1.3 300 mesh copper grids and plunge frozen in liquid ethane after a two-sided blot using a FEI Vitrobot. Vitrified helical tubes were imaged in low-dose mode on a FEI Tecnai G2 Sphera LaB$_6$ at 200 kV using a 4k x 4k FEI Eagle Camera. RELION 2.0.4 was used for 2D classification of manually selected helical segments.

Molecular dynamics simulation

The filament subunits were represented by the 3-beaded model, as previously developed by us (Harker-Kirschneck et al., 2019). The target geometry of the protein filaments was a ring, which was controlled by the 9 bonds between consecutive filament subunits. By setting the equilibrium bond lengths to different values, the first filament was targeted as a flat ring ($\tau_1 = 0$, Figure S4B) and the second filament a tilted ring ($\tau_2 = 90$, Figure S4B). The tilt angle τ is defined as the angle between the radial axis and the triplet subunit axis (see Figure 2a in Harker-Kirschneck et al., 2019).

Force constants for the bonds between filament subunits were set as $k_1 = k_2 = 48 \cdot k_B T / nm^2$ (Figure 5C) or $k_1 = 24 \cdot k_B T / nm^2$, $k_2 = 48 \cdot k_B T / nm^2$ (Figure S4A). The central angle between neighboring filament subunits was set as $\alpha_0 = 15°$, so that the target radius R equals 13.2 (15.8) nm for the first (second) filament. R is defined as the in-plane distance between the center of the ring to the center of mass of each subunit. Lennard-Jones (LJ) potential ($r_c = 1.3 \cdot r_{min}$, $\varepsilon_1 = \varepsilon_2 = 3.0\ k_B T$ (Figures 5C and S4A, left panel), $\varepsilon_1 = 2.0\ k_B T$, $\varepsilon_2 = 4.0\ k_B T$ (Figure S4A, right panel)) was applied to mimic the binding interfaces between the two bottom beads of each filament subunit (light green, light purple) and all membrane beads (gray), as well as the bottom beads at the interface of the two filaments. Volume exclusion potential ($\varepsilon = 2.0\ k_B T$, $r_c = r_{min}$) was applied to all other pairs of protein beads. ε is the depth of the LJ potential, k_B is the Boltzmann constant, T is the temperature, r_c is the LJ cut off distance, r_{min} is the distance at the potential minimum. The membrane was represented by the one-bead-thick model in the fluid state (Yuan et al., 2010) with parameters $\varepsilon = 4.34\ k_B T$, $\mu = 3.0$, $\xi = 4.0$, $\theta_0 = 0°$ following the notation in the original paper. For the simulation of the disassembly of the second filament, we manually set all bonded and non-bonded interactions of this filament within itself and with other part of the system to zero. All beads were in the same size (diameter $d = 2.3$ nm).

The filaments were initialized as a set of loosely-packed double-stranded spiral in the flat state, with each filament constructed of 186 subunits. The individual filament subunits were set as rigid bodies. A layer of 7360 membrane beads (184 × 184 nm^2) were laid under the filaments in the x-y plane (see Figures S4C–S4E). Periodic boundary condition was applied to all directions. The box size in z direction was set to 2300 nm to avoid the periodic boundary effect in this direction. Time step was set as 0.01 t_0, where t_0 is the reduced time unit. The simulation was performed in the NPH ensemble with the barostat targeted at zero pressure to model a membrane with a low tension (Harker-Kirschneck et al., 2019). The Langevin thermostat was applied at each time step to model Brownian diffusion at the room temperature. Initially, the membrane was equilibrated for 10,000 steps with the protein filaments kept frozen. The protein filaments were then released with both filaments targeted at $\tau = 0$. We then changed the target geometry of the second filament to the $\tau_2 = 90$ state, while made no change to the $\tau_1 = 0$ filament. Finally, the $\tau_1 = 0$ filament was disassembled and only the $\tau_2 = 90$ was kept on the membrane.

QUANTIFICATION AND STATISTICAL ANALYSIS

SBL-bilayer assay and membrane necks

For quantification of supported bilayer experiments, integrated fluorescence intensity of single patches was measured, normalized to either their maximum or time point 0 and a kymograph was extracted. For artificial membrane neck experiments, sections containing membrane necks were selected manually, linearized and integrated fluorescence intensity was measured along the contour and/or through time using Fiji. Fluorescence intensities were normalized by their maximum value. To determine the colocalization of Alexa488-Snf7 and Atto647N-DOPE peaks, relative fluorescence was measured along linearized membrane contours after smooth averaging, relative fluorescence values were binarized (1 above threshold, 0 below, thresholds: 0.3 Snf7, 0.4 DOPE). The percentage of no colocalization was extracted by the proportion of pixels with the value 1 from the Snf7 channel for which the value in the membrane channel was 0. No colocalization was only counted at a minimal distance of four pixels to the nearest membrane neck (value 1). For all experiments the mean and standard deviation (SD) were calculated. Number of independent experiments (n) und number of patches or membrane necks (ROI) analyzed are indicated in the corresponding figure legends. The graph and statistics were done using Prism 8 (GraphPad software).

Cryo electron microscopy

RELION 2.0.4 was used for 2D classification of manually selected helical segments.

Confocal imaging of mammalian cells

For the analysis, the spots were detected for each frame for both channels using the spot detector plugin in Icy software and exported as ROIs. For each time point the sum of dots mean intensity was calculated using Excel, the value obtained before the shock was

subtracted and the curve was normalized to 1 (for its maximum value). The graph and statistics were done using Prism 8 (GraphPad software). Mean and standard error of the mean (SEM) were calculated. Number of independent experiments (n) und number of spots (ROI) used in the analysis are indicated in the figure legend.

Molecular dynamics simulation

The duration of the last three production runs were ~1,000,000 steps each. The molecular dynamics simulations were carried out with Lammps code (https://lammps.sandia.gov) (Plimpton, 1995). The invagination depth was calculated by taking the z coordinate difference in the average of highest 5000 and the average of lowest 5 membrane particles.
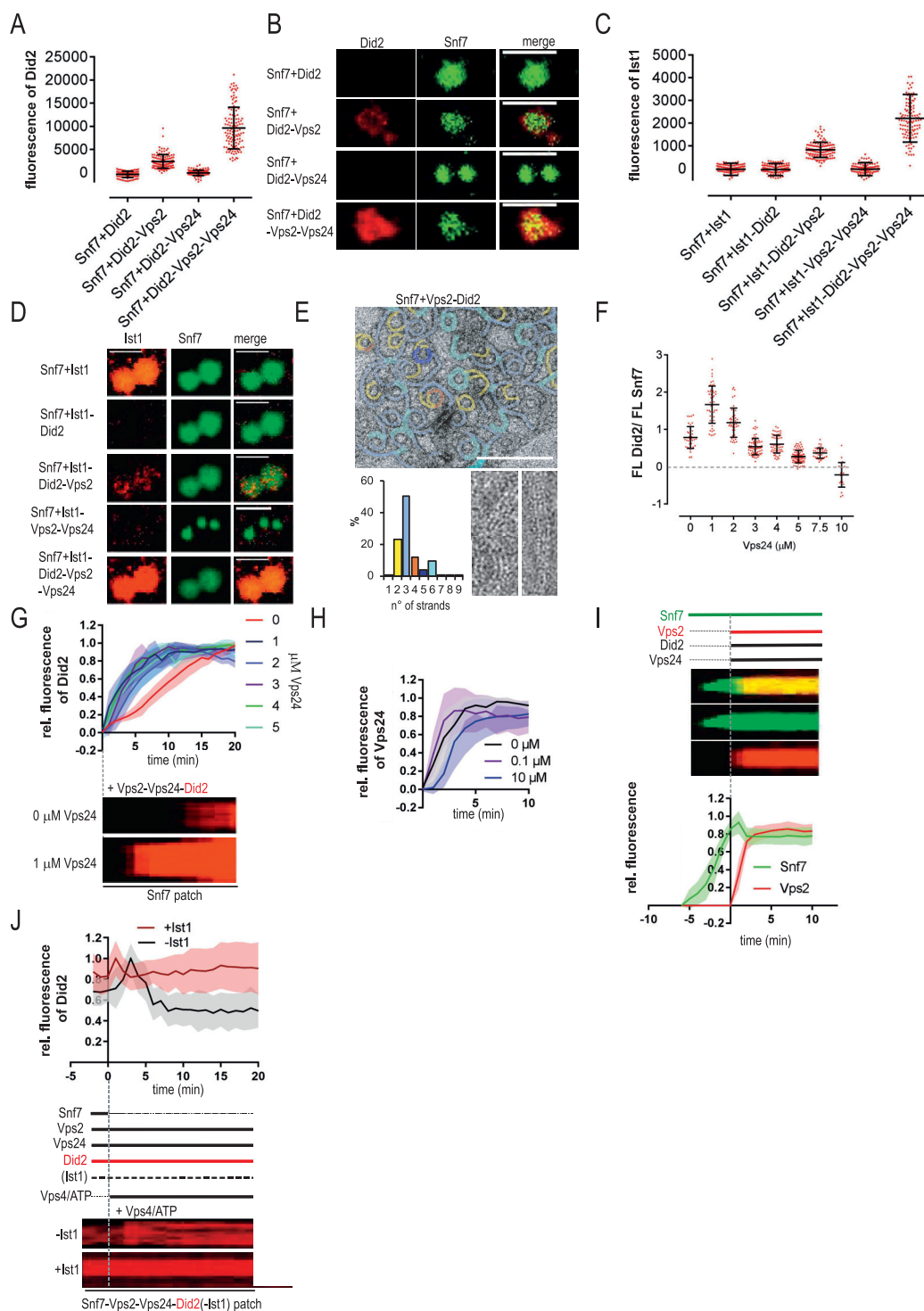
Supplemental Figures

Figure S1. Vps2 and Did2 Form a Snf7-Binding Complex, Related to Figures 1, 2, and 3

A-B. Confocal images and quantification of Atto565-Did2 fluorescence of LUVs or Snf7-covered LUVs incubated with Atto565-Did2 and the indicated proteins (scale bar 10 μm n ≥ 3; mean ± SD). C-D. Confocal images and quantification of Atto565-Ist1 fluorescence of LUVs or Snf7-covered LUVs incubated with

(legend continued on next page)

Atto565-Ist1 and the indicated proteins (scale bar 10 μm n $\geq$ 3; mean $\pm$ SD). E. Negative stain electron micrographs of ESCRT-III filaments polymerized on LUVs. Histograms show the distribution of number of strands per bundle (scale bar: 100nm). F-G. Kymographs and fluorescence quantification of patch assay in which Atto565-Did2, Vps2 and indicated amount of Vps24 was added at t = 0 min to pre-grown Alexa488-Snf7-patches. Atto565-Did2 fluorescence was plotted against time (n = 3, ROI $\geq$ 55; mean $\pm$ SD). Ratio of Atto565-Did2 to Alexa488-Snf7 fluorescence at plateau was plotted against Vps24 concentration. H. Fluorescence quantification of Snf7-patch assays in which Alexa488-Vps24, Vps2 and indicated amount of Did2 were added at t = 0 min to pre-grown Snf7-patches. Alexa488-Vps24 fluorescence was plotted against time (n = 3; mean $\pm$ SD). I. Kymographs and fluorescence quantification of Snf7-patch assays without Vps4/ATP. Color code stands for protein label, green: Alexa488, red: Atto565, black: no label. ESCRT-III proteins were added at indicated time points (gray dash line) (n = 3 ROI = 109; mean $\pm$ SD). J. Kymographs and fluorescence quantification of patch assay in which Vps4/ATP was added at t = 0 min to pre-grown Snf7-patches pre-incubated with Vps24, Vps2 and Atto565-Did2 in presence or absence of Ist1. Atto565-Did2 fluorescence was plotted against time. (-Ist1: n = 3, ROI = 188; +Ist1: n = 4, ROI = 201; mean $\pm$ SD).
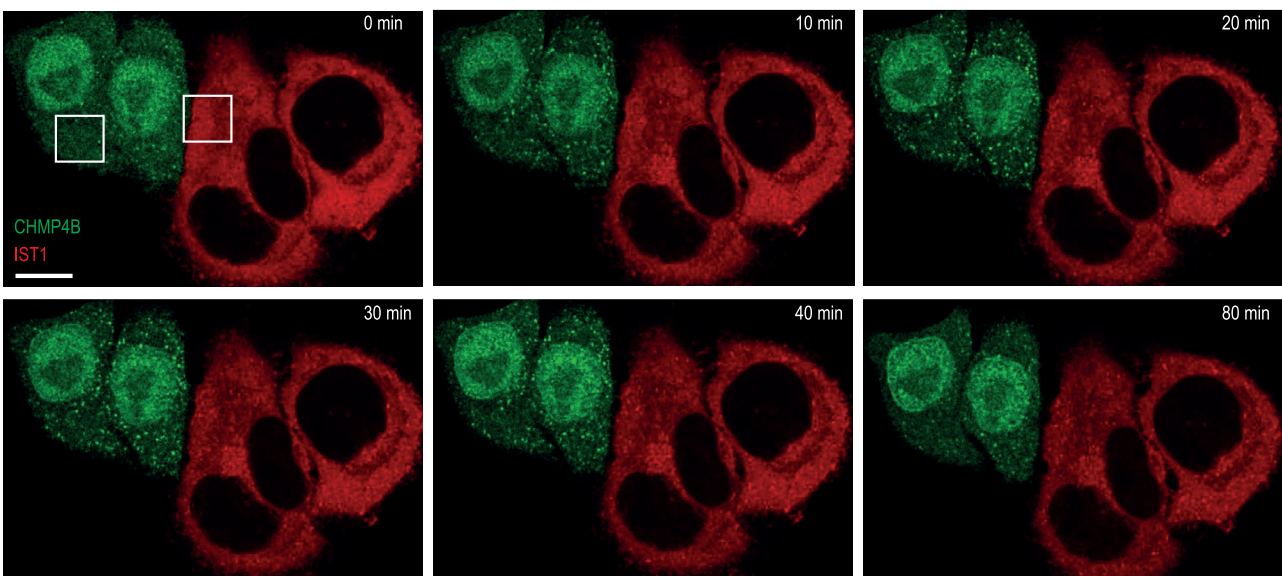
A
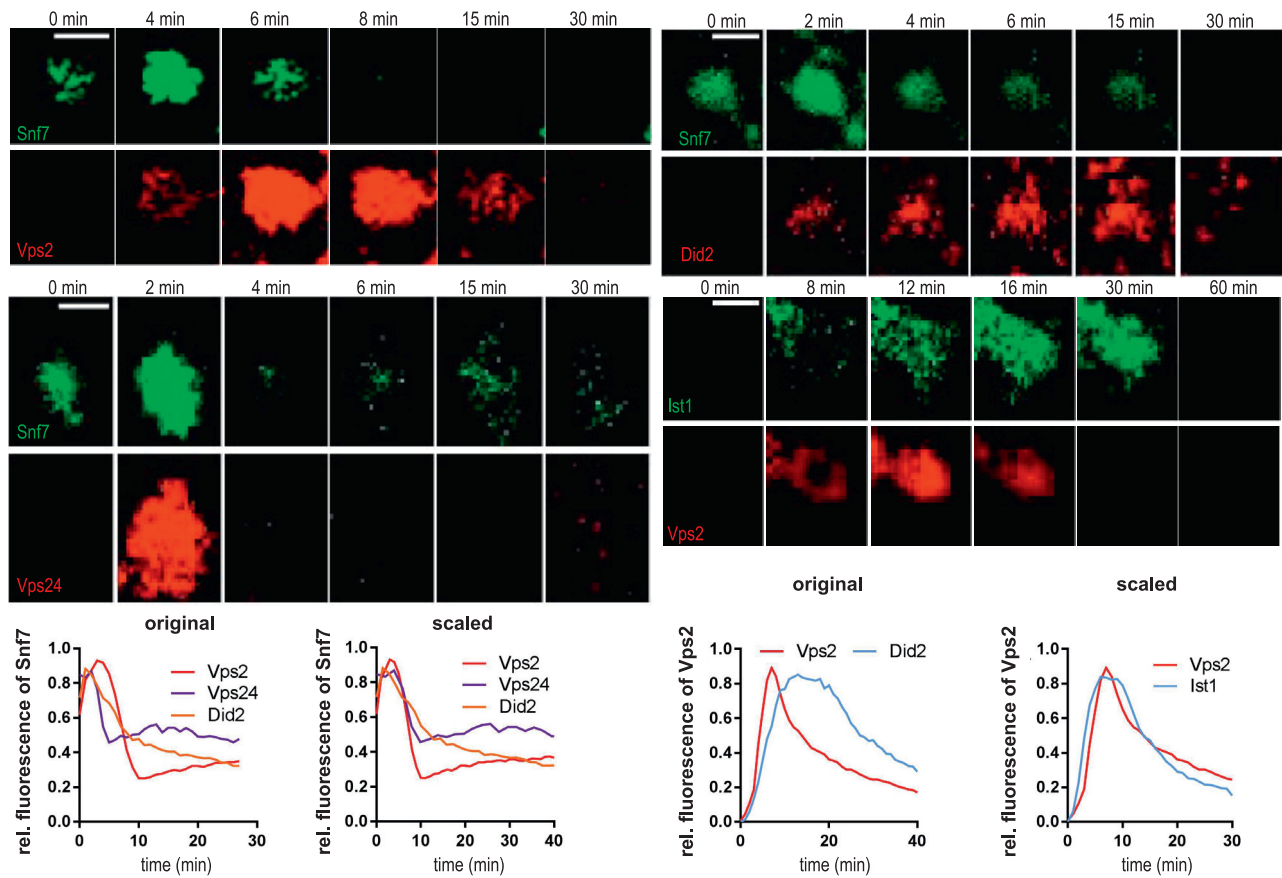
B

Figure S2. Vps4 Drives a Polymerization Sequence of ESCRT-III Subunits, Related to Figure 4

A. Confocal images of experiments described in Figure 4A. Snf7, Vps2, Vps24, Did2, Ist1,Vps4 and ATP were added to pre-grown Alexa488-Snf7 patches at t = 0 min. Fluorescence of Alexa488-Snf7 and Atto565-Vps2 (n = 3 ROI = 108; mean ± SD) or Atto565-Vps24 (n = 3 ROI = 65; mean ± SD) or Atto565-Did2 (n = 3

(legend continued on next page)

ROI = 55; mean ± SD) was monitor and Alexa488-Snf7 fluorescence plotted against time (scale bar 2 μM). Alexa488-Snf7 fluorescence graphs were scaled und aligned. Fluorescence of Atto565-Vps2 and Alexa-Ist1 (n = 4 ROI = 71; mean ± SD) was monitor and Atto565-Vps2 fluorescence plotted against time (scale bar 2 μM). Atto565-Vps2 fluorescence graphs were scaled und aligned (see Methods for further description).

B. Life-cell imaging of endosomal recruitment of CHMP4B-GFP and IST1-mcherry after hypertonic shock (HS). HS was applied at t = 0 min. Framed area is shown in Figure 4B (scale bar 10 μm; CHMP4B: n = 3, ROI = 37; IST1: n = 3, ROI = 43).
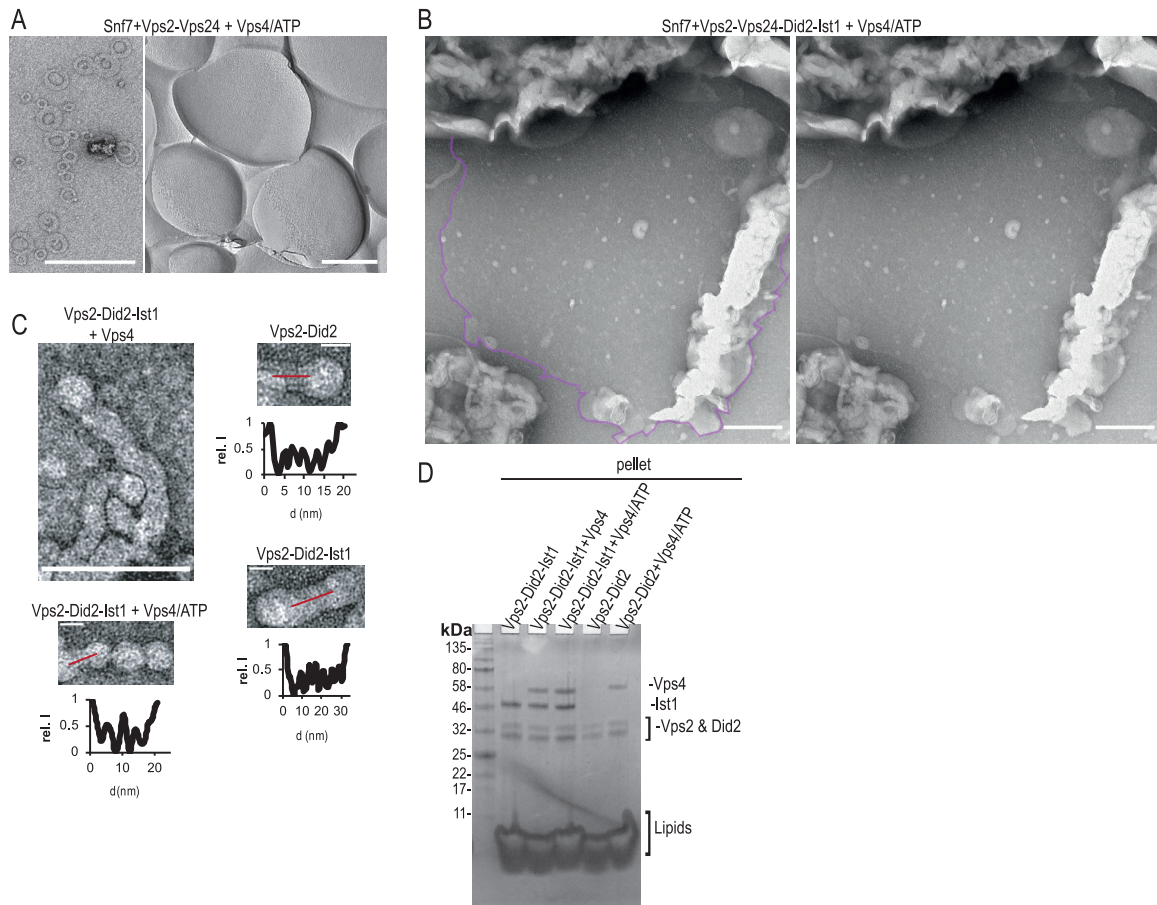
Figure S3. ESCRT-III Polymerization Sequence Drives Filament Deformation and Constriction, Related to Figures 5 and 6
A. Negative stained and freeze fracture micrographs of LUVs incubated with the indicated proteins (scale bar 100 nm). B. Negative stained micrographs of LUVs described in Figure 6A. LUVs were incubated with Snf7, Vps2, Vps24, Did2, Ist1 and Vps4/ATP (scale bar 200 nm) and outline of a burst LUV was traced (left panel, original image right panel).C. Negative stained micrographs of LUVs incubated with the indicated proteins described in Figure 6B (scale bar 100nm zoom 20 nm). Filament profiles were analyzed by measuring intensities along the overlaid line. D. Comassie-staining of SDS-PAGE loaded with the pellet after ultra-centri-fugation of LUVs incubated with the indicated proteins.
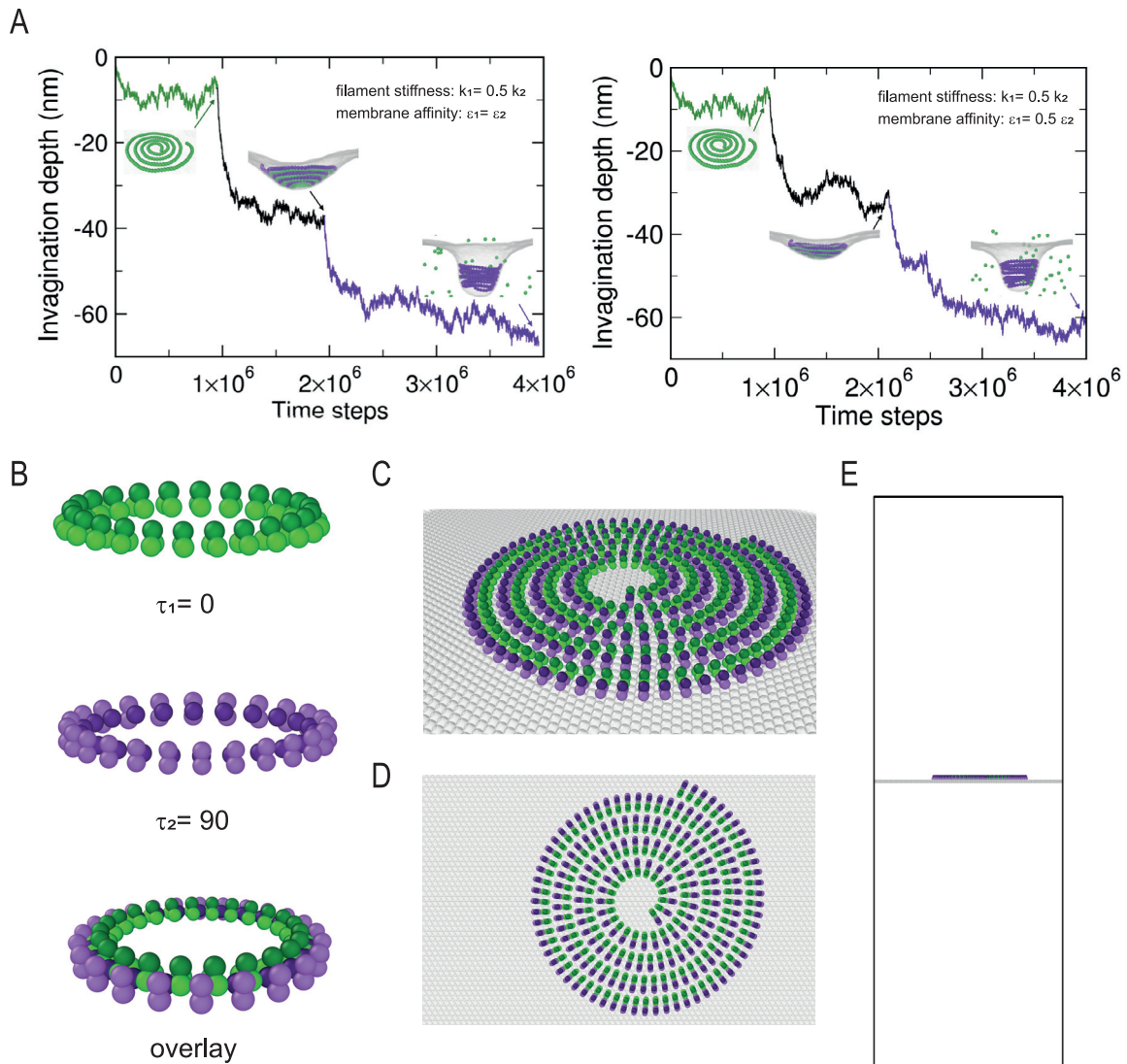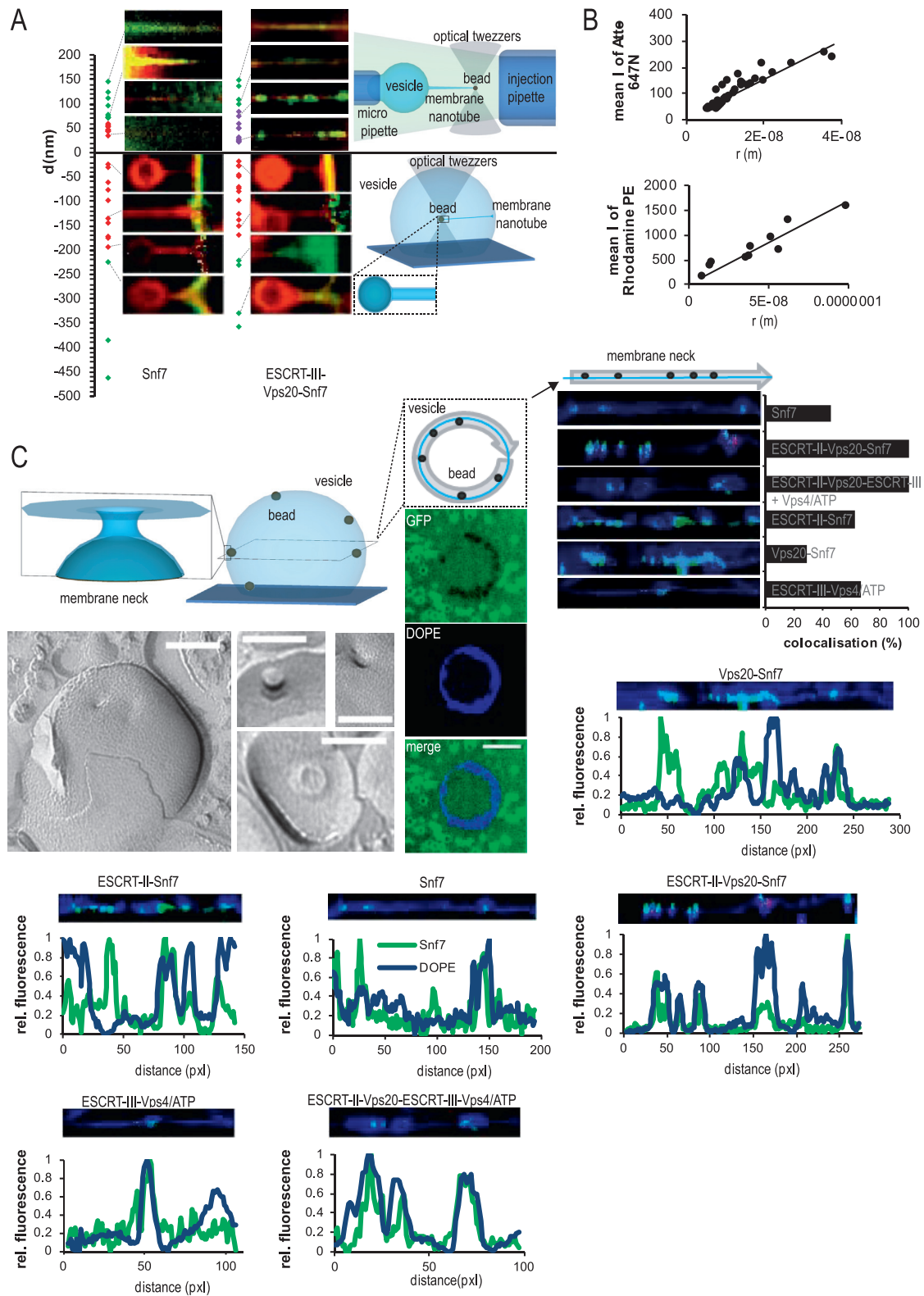
Figure S4. ESCRT-III Polymerization Sequence Drives Filament Deformation, Related to Figure 5

A. Membrane invagination depth estimated by molecular dynamics simulation of sequential assembly and disassembly of two filaments with different filament tilts with respect to the membrane surface ($\tau_1 = 0$, flat, $\tau_2 = 90$, tilted). B. Target geometry for the flat state ($\tau_1 = 0$), the tilted state ($\tau_2 = 90$), superposition of flat and tilted state. C-E: Initial structure for the molecular dynamics simulation. C, D, E are perspective, top, front view, respectively. Green, purple beads represent the first and the second filament, respectively. Dark colors represent the top beads and light colors represent the bottom beads for each filament subunit. Membrane beads are depicted in gray.

A

d(nm)

Snf7

ESCRT-III-Vps20-Snf7

optical twezzers

vesicle bead injection pipette
micro pipette membrane nanotube

optical twezzers

vesicle bead membrane nanotube

B

mean I of Atte 647N

r (m)

mean I of Rhodamine PE

r (m)

C

membrane neck

vesicle bead

vesicle

bead

membrane neck

membrane neck

GFP

DOPE

merge

Snf7

ESCRT-II-Vps20-Snf7

ESCRT-II-Vps20-ESCRT-III
+ Vps4/ATP

ESCRT-II-Snf7

Vps20-Snf7

ESCRT-III-Vps4/ATP

colocalisation (%)

Vps20-Snf7

rel. fluorescence

distance (pxl)

ESCRT-II-Snf7

rel. fluorescence

distance (pxl)

Snf7

Snf7
DOPE

rel. fluorescence

distance (pxl)

ESCRT-II-Vps20-Snf7

rel. fluorescence

distance (pxl)

ESCRT-III-Vps4/ATP

rel. fluorescence

distance (pxl)

ESCRT-II-Vps20-ESCRT-III-Vps4/ATP

rel. fluorescence

distance(pxl)

(legend on next page)

Figure S5. ESCRT-II and Vps20 Site-Specifically Nucleates ESCRT-III Polymers at Artificial Membrane Necks, Related to Figure 7

A. Outward (upper panel) and inward (lower panel) pulled membrane nanotubes were incubated with indicated proteins. Binding of Alexa488-Snf7 was plotted against the diameter of the membrane tubes (green, binding; red, not binding; purple, nucleation of large aggregates). B. Calibration curves for calculation of radii of inward-directed membrane tubes. Mean fluorescence of outward-directed membrane nanotubes were plotted against radii calculated from bead displacement. C. Micrographs of freeze-fractured LUVs containing artificial membrane necks (scale bar 100 nm) and confocal images of GUV containing artificial membrane necks incubated with GFP (scale bar 5 μm). Schematic representation of artificial membrane necks assay with beads engulfed in GUVs and linearized contour of GUVs taken from confocal images of membrane necks incubated with the indicated proteins. Relative intensities of Atto647N-DOPE and Alexa488-Snf7 was measured along the contours. Colocalization of Alexa488-Snf7 with artificial membrane necks (Atto647N-DOPE peaks) was quantified by measuring of the percentage of positions with both Atto647N-DOPE and Alexa488-Snf7 intensities above a threshold value along the contour.
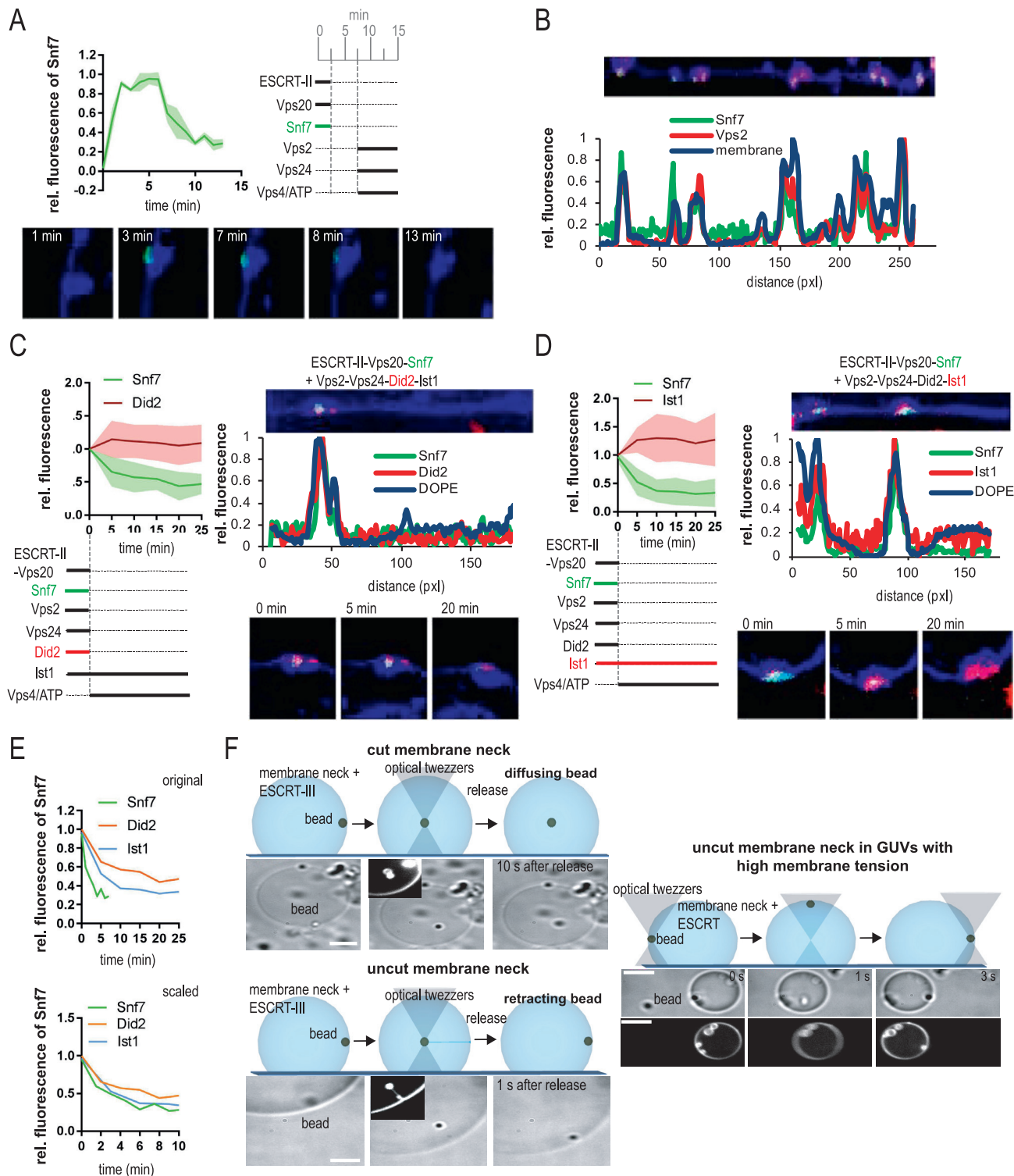
Figure S6. ESCRT-III Polymerization Sequence Drives Fission of Artificial Membrane Necks, Related to Figure 7

A . Fluorescence quantification of artificial membrane necks incubated with the indicated sequence of proteins. Relative intensity of Alexa488-Snf7 was measured over time. B. Linearized contour of GUVs and fluorescence quantification of artificial membrane necks incubated with the indicated sequence of proteins. Relative intensities of Atto647N-DOPE, Alexa488-Snf7 and Atto565-Vps2 was measured along the contours. C. Linearized contour of GUVs, confocal images and fluorescence quantification of artificial membrane necks incubated with the indicated sequence of proteins. Vps4/ATP was added at t = 0 min to

(legend continued on next page)

pre-grown Alexa488-Snf7 structures pre-incubated with Atto565-Did2, Vps2, Vp24 and Ist1. Relative intensities of Atto647N-DOPE, Alexa488-Snf7 and Atto565-Did2 was measured along the contours and over time (n = 3, ROI = 20; mean ± SD). D. Linearized contour of GUVs, confocal images and fluorescence quantification of artificial membrane necks incubated with the indicated sequence of proteins. Vps4/ATP was added at t = 0 min to pre-grown Alexa488-Snf7 necks structures pre-incubated with Atto565-Ist1, Vps2, Vp24 and Did2. Relative intensities of Atto647N-DOPE, Alexa488-Snf7 and Atto565-Ist1 was measured along the contours and over time (; mean ± SD). E. Scaling of ESCRT-III polymerization sequence at artificial membrane necks. Alexa488-Snf7 fluorescence graphs were scaled und aligned (see Methods for further description). F. Schematic representation of membrane fission assay. Experiment was performed as describ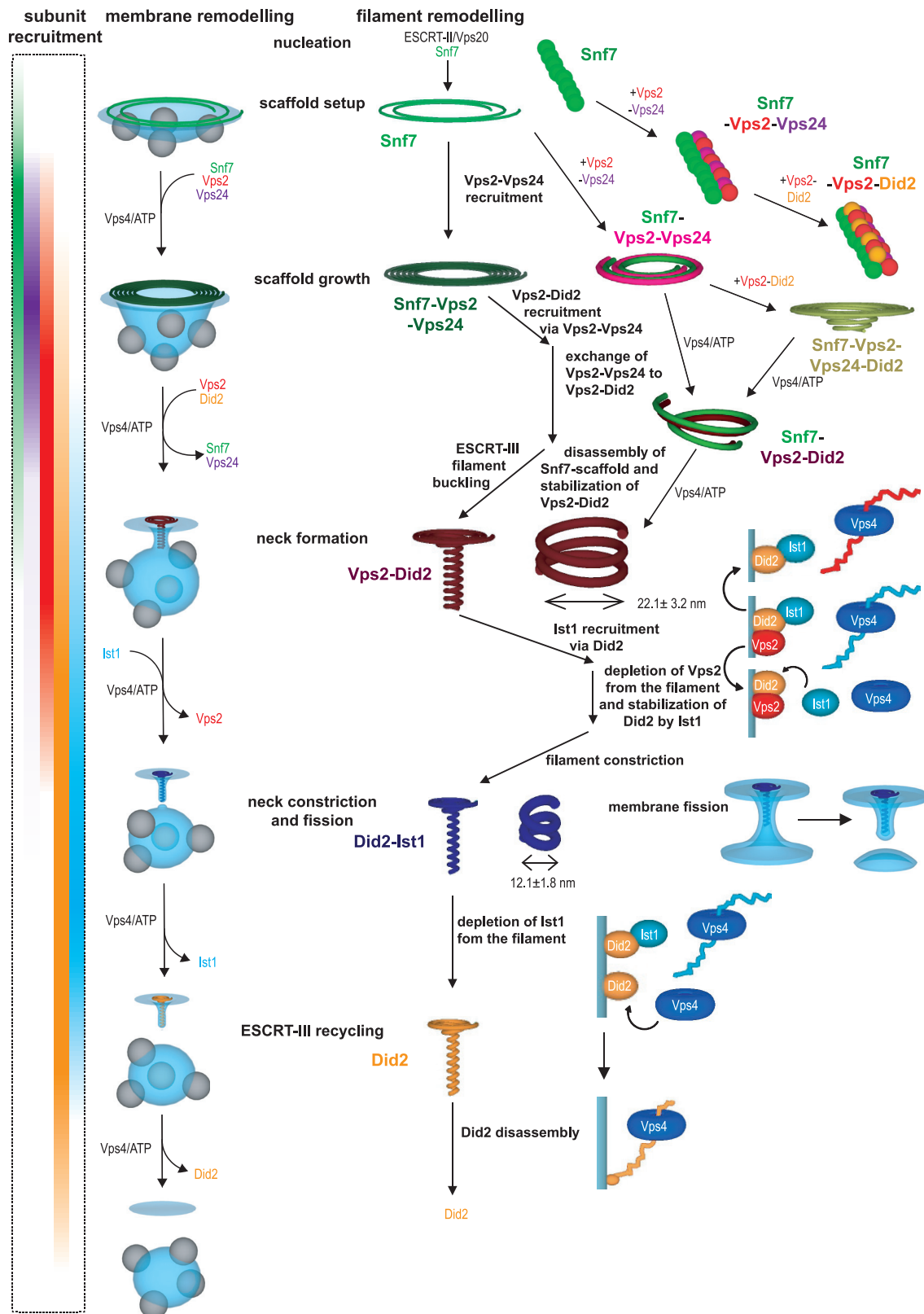ed in Figure 7C (scale bar: 5 μm).